

Geochemistry, Geophysics, Geosystems®



RESEARCH ARTICLE

10.1029/2023GC011344

Characterization of Southern Peru Hydrothermal Systems: New Perspectives for Geothermal Exploration Along the Andean Forearc

Key Points:

- The geochemical properties of Southern Peru's hot springs are influenced by their spatial correlation with volcanic or tectonic features
- By combining permeable faults and topography, 3D hydrothermal modeling replicates the temperatures and locations of observed springs
- Detection of regional topography-driven thermal plumes along faults in the Andean forearc opens perspectives for geothermal exploration

Audrey Taillefer¹ , Laurent Truche¹, Laurence Audin¹ , Frédéric-Victor Donzé¹ , Delphine Tisserand¹, Simona Denti¹, Nelida Manrique Llerena², Pablo Jorge Masías Alvarez² , Régis Braucher³ , Swann Zerathe¹ , Christophe Monnin⁴ , Hugo Dutoit¹ , Edu Taïpe Maquerhua² , and Fredy Erlington Apaza Choquehuayta²

¹University Grenoble Alpes, University Savoie Mont Blanc, CNRS, IRD, University Gustave Eiffel, ISTerre, Grenoble, France, ²Instituto Geológico Minero y Metalúrgico (INGEMMET), Arequipa, Perú, ³Université Aix-Marseille, CNRS-IRD-Collège de France-INRAE, UM 34 CEREGE, Technopôle de l'Environnement Arbois-Méditerranée, Aix-en-Provence, France, ⁴Géosciences Environnement Toulouse (GET), Université de Toulouse, CNRS, IRD 14 Avenue Edouard Belin, Toulouse, France

Supporting Information:

Supporting Information may be found in the online version of this article.

Correspondence to:

A. Taillefer,
audrey.taillefer@gmail.com

Citation:

Taillefer, A., Truche, L., Audin, L., Donzé, F.-V., Tisserand, D., Denti, S., et al. (2024). Characterization of Southern Peru hydrothermal systems: New perspectives for geothermal exploration along the Andean forearc. *Geochemistry, Geophysics, Geosystems*, 25, e2023GC011344. <https://doi.org/10.1029/2023GC011344>

Received 17 NOV 2023

Accepted 26 MAR 2024

Author Contributions:

Conceptualization: Audrey Taillefer, Laurent Truche, Laurence Audin, Frédéric-Victor Donzé, Nelida Manrique Llerena

Data curation: Audrey Taillefer

Formal analysis: Audrey Taillefer, Delphine Tisserand, Simona Denti, Pablo Jorge Masías Alvarez, Christophe Monnin

Abstract This study provides a comprehensive characterization of various hydrothermal systems in Southern Peru ranging from the faulted Precordillera's steep topography up to the volcanic High Cordillera (>4,000 m asl). The objective is to investigate thermal anomalies that may potentially serve as new geothermal resources. Our integrated approach combines: (a) geochemistry from 14 hot springs sampled throughout the Tacna region, and (b) 3D numerical modeling of coupled groundwater and heat transfer considering topography and faults embedded in homogeneous permeability. Water and gas analysis indicates that the springs located near volcanoes discharge Na-K-Cl waters with high temperatures (>87°C), high Total Dissolved Solid concentrations (TDS >3,452 mg/L), and free gases dominated by CO₂ (>90 vol%). Springs located along the regional faults in the Precordillera discharge Ca-SO₄ and Na-K-Cl waters with moderate temperatures (27–53°C), intermediate TDS concentrations (464–2,458 mg/L), radiocarbon ages between 1.4 and 7.9 kyr, and free gases dominated by N₂ (>95 vol%). The Aruma springs, which are located at the transition between the High and the Precordillera, display intermediate characteristics. Numerical models accurately replicate the locations and temperatures of the fault-related springs only for permeable faults (>10⁻¹⁴ m²), revealing the creation of 100-km long thermal plumes along faults, locally rising up the 150°C-isotherm to about ~1,000 m below the surface. This approach clearly distinguishes the spring origins, which are volcanic in High Cordillera and tectonic in Precordillera. Moreover, we highlight that steep topographic gradient and permeable reverse faults in the Andean forearc may generate considerable thermal anomalies, opening perspectives for the geothermal exploration.

Plain Language Summary Geothermal energy is an essential part of the transition to green energies. It consists of using the Earth's natural heat to generate electricity or provide direct heating. In the Peruvian Andes there is significant geothermal potential near volcanoes that constitute an efficient heat source. However, these are distant from many of the population hubs, mostly located along the Pacific Coast. In the Tacna region, Southern Peru, we observe hot springs aligned along faults near the city. We hypothesize that these faults act as pipes for the hot fluids making them suitable for geothermal energy extraction. The geochemical compositions of various hot springs in the region are compared with 3D numerical models simulating hydrothermal flows. We found that springs along volcanoes and those along faults have different geochemical signatures, evidencing different subsurface pathways. Numerical models accurately replicate the positions and temperatures of the observed and sampled hot springs and reveal significant thermal anomalies around compressional faults. Our findings open up promising perspectives for the geothermal exploration in the Andean forearc.

1. Introduction

The energy mix in Peru is dominated by fossil fuels (>72%), while the renewable part other than hydropower is negligible (4.4%, <https://ourworldindata.org/>). The enhancement of renewable energy along the Andean Cordillera requires the development of the geothermal energy that is non-intermittent and locally available.

© 2024 The Authors. *Geochemistry, Geophysics, Geosystems* published by Wiley Periodicals LLC on behalf of American Geophysical Union.

This is an open access article under the terms of the [Creative Commons Attribution-NonCommercial-NoDerivs License](https://creativecommons.org/licenses/by/4.0/), which permits use and distribution in any medium, provided the original work is properly cited, the use is non-commercial and no modifications or adaptations are made.

Funding acquisition: Audrey Taillefer, Laurent Truche, Laurence Audin, Frédéric-Victor Donzé

Investigation: Audrey Taillefer, Laurent Truche, Laurence Audin, Frédéric-Victor Donzé, Delphine Tisserand, Simona Denti, Nelida Manrique Llerena, Pablo Jorge Masías Alvarez, Régis Braucher, Swann Zerathe, Hugo Dutoit, Edu Taïpe Maquerhua, Fredy Erlington Apaza Choquehuayta

Methodology: Audrey Taillefer, Laurent Truche, Laurence Audin, Delphine Tisserand, Simona Denti, Pablo Jorge Masías Alvarez, Christophe Monnin
Project administration: Audrey Taillefer

Resources: Laurent Truche, Delphine Tisserand, Simona Denti, Nelida Manrique Llerena, Régis Braucher, Swann Zerathe

Software: Audrey Taillefer

Supervision: Laurent Truche, Laurence Audin, Frédéric-Victor Donzé, Simona Denti

Validation: Audrey Taillefer, Laurent Truche

Visualization: Audrey Taillefer

Writing – original draft:

Audrey Taillefer

Writing – review & editing:

Laurent Truche, Laurence Audin, Frédéric-Victor Donzé, Delphine Tisserand, Simona Denti, Nelida Manrique Llerena, Swann Zerathe, Christophe Monnin

Assessing the geothermal potential for energy production involves understanding the underlying geological processes to identify suitable locations in unexplored geological contexts.

At first order, the evaluation of geothermal potential is based on surface indicators of thermal anomalies, such as hot springs, geysers and fumaroles (Stelling et al., 2016). In the context of subduction, two main types of geothermal systems can be found: volcanic and orogenic belt systems (Moeck, 2014).

In volcanic systems, the magmatic chambers below the volcanic edifices supply direct heat to the meteoric fluids circulating nearby, leading to superficial manifestations of geothermal activity (e.g., Hochstein (1988)). The geothermal reservoir is typically constituted by an upflow zone tightly coupled to the thermal anomaly generated by the magmatic chamber (e.g., Tarapa in Java, Intani et al. (2020); Taupo in New-Zealand, C. J. Wilson and Rowland (2016)), and represents the principal geothermal targets over the globe (Moeck, 2014).

In the orogenic belt type, no abnormal heat source such as volcanic activity is required. Instead, local geothermal gradients and heat flows, themselves influenced by the radiogenic heat production, the rock rheology, the tectonic regime, and the topography, constitute the heat source and flow path of hot fluids (Guillou-Frottier et al., 2024). The combination of free-convection along permeable faults (Belgrano et al., 2016; Guillou-Frottier et al., 2020) and forced-convection induced by topographic gradients (Sutherland et al., 2017; Volpi et al., 2017; Wanner et al., 2019) ensures fluid circulation between the surface and the great depths in the forearc (Forster & Smith, 1989; López & Smith, 1995). Faulted forearcs would also constitute a geothermal reservoir (Grasby & Hutcheon, 2001) but they are not yet considered as an economical target (e.g., Jolie et al. (2021)). The interactions between heat sources and fluids involved becomes complex in regions where faulted forearc meets high volcanic ranges (e.g., Pearce et al., 2020; Veloso et al., 2020; Wrage et al., 2017).

In the Tacna region, South of Peru, seven clusters of hot springs are located in the volcanic High Cordillera and active faults along the Precordillera (Figure 1). In the volcanic arc, the geothermal potential is high, and associated with the active volcanoes (Cruz & Vargas, 2015; Lahsen et al., 2015; Vargas & Cruz, 2010). However, these high-altitude zones (>4,000 m above sea level asl) are located at considerable distances (>50 km) from the main population hubs and centers of energy demand, which are predominantly located in the forearc basin near the Pacific coast, in this case the active Andean forearc. At lower altitude (below 2,000 m asl), hot springs are aligned along active faults where significant topographic gradients mark the limit between the Precordillera and the arid forearc basin named the Central Depression. These hot springs provide evidences of geothermal circulations at a considerable distance from active volcanoes. Occurrence of hot water throughout the Western High Cordillera and active tectonic belt to the coast, challenge our comprehension of the geothermal potential at the regional scale: how do thermal anomalies develop, where are they localized in southern Peru and what are the respective contributions of the volcanic and tectonic processes that allow fluid heating, recharge, and circulations ?

This study aims to assess the geothermal potential of the Tacna region by investigating the influence of volcanoes, faults, and steep topographic gradients on hydrothermal circulation. Given the complexity of the area and the limited depth-related data available, we have employed two complementary approaches: field data collection and regional-scale numerical modeling of hydrothermal systems. Our methodology involves gathering new field data and conducting geochemical analyses of water and gas compositions from a series of hot springs. This analysis will enable us to characterize various aspects of the hydrothermal systems, including their composition, origin, the elevation of recharge areas, ages, and reservoir temperatures. Moreover, it will help us establish connections between these systems, volcanoes, faults, and each other. In a complementary approach, we have developed a 3D numerical model of hydrothermal circulation using topographical data extracted from a Digital Elevation Model and structural geometry derived by the geological context. This model facilitates the investigation of the thermal regime within both fault and host rocks, the assessment of the permeability of faults, the understanding of fluid circulations induced by topographical features, and the characterization of associated thermal anomalies. Validation of the model relies on two key parameters: the locations and temperatures of the springs obtained from our field data collection. By comparing these parameters with the model predictions, we ensure the accuracy and reliability of the model. The combined information obtained through these two methods enables us to propose a comprehensive conceptual model of the regional-scale hydrothermal systems to initiate a discussion on exploring the geothermal potential associated with forearc reverse faults.

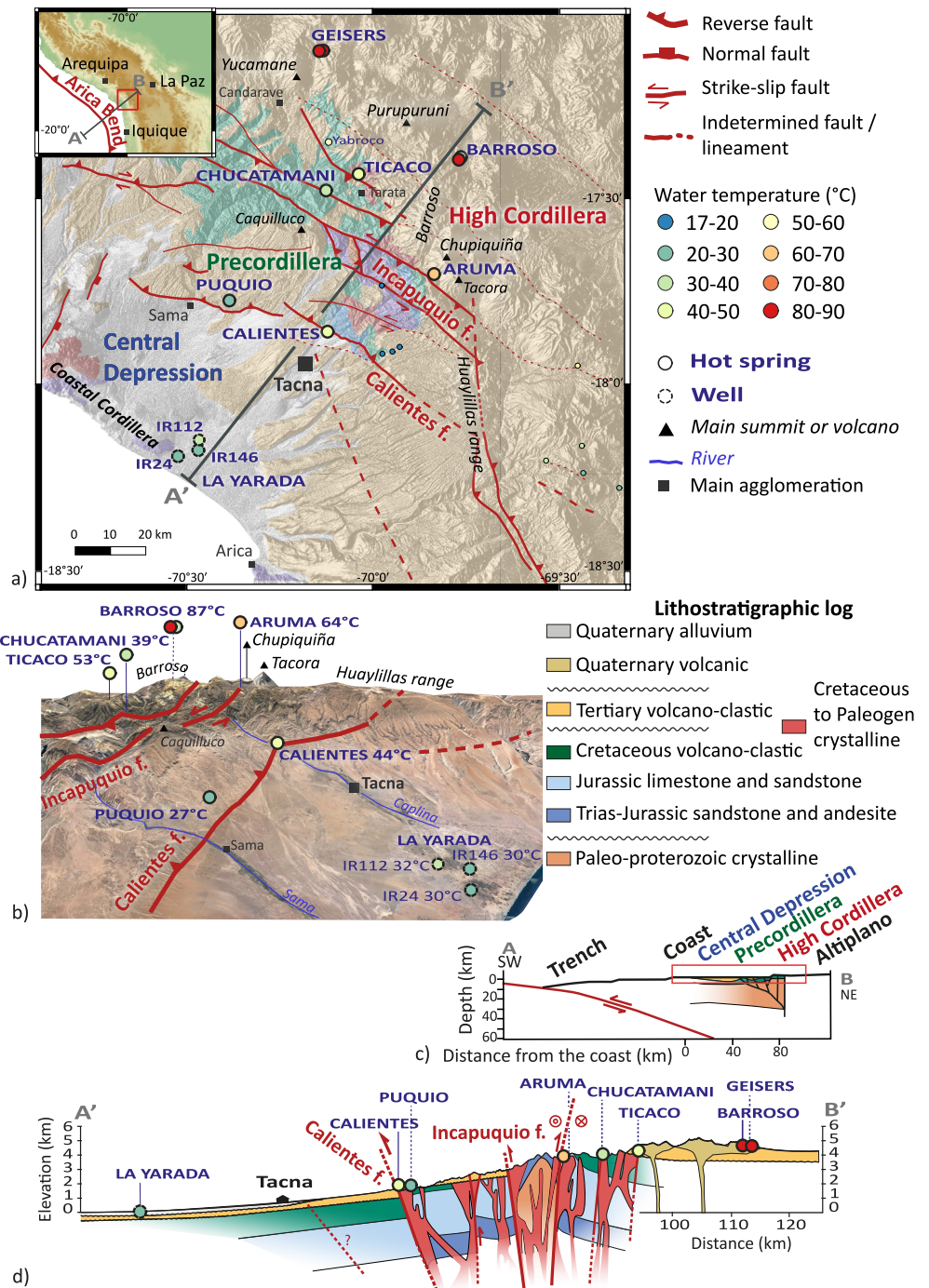


Figure 1. Location and temperatures of the sampled hot springs and wells in the study area. Simplified lithostratigraphic log in legend. (a) Geological map with superimposed shading (270° of lighting) from a 30 m-DEM (ALOS), after the INGEMMET geological map (<https://geocatmin.ingemmet.gob.pe/geocatmin/>), Audin et al. (2006), Van Zalinge et al. (2017), Benavente et al. (2017), Alván et al. (2018), Benavente et al. (2022), and García et al. (2022), and field data, (b) Topographic view (x3 of vertical exaggeration, Google Earth) from the NW, (c) Large-scale AA' cross-section modified after Hall et al. (2012), (d) Interpreted regional cross-section BB' after (a, c) (x10 of vertical exaggeration).

2. Hydro-Geological Setting

2.1. General Geological Setting

We describe here the topography, lithology, faulting and tectonic regime in the study area, which are critical parameters that influence hydrothermal circulation (Guillou-Frottier et al., 2024). These parameters will further be used for the design of the hydrothermal model. A subsequent description of the geological context of the studied springs, geysers, and wells allows to relate them to the previously described regional features.

2.1.1. Geomorphological Setting

The study area is located at the -18°S latitude South of Peru, close to the border with Chile, in the region of Tacna (320,000 inhabitants in 2005, Figure 1). This area is representative of the ongoing orogenic processes that have built the Andean topography, which is related to the subduction of the Nazca plate beneath the South American plate for 80 Myr (Chen et al., 2019; Pardo-Casas & Molnar, 1987). The building of the topography accelerated during the Neogene as well as the activity of the main tectonic structures (Schepers et al. (2017) and ref. therein). In planar view, the subduction geometry forms a 120° bend pointing toward the East, known as the Arica Bend (Figure 1a). This bend constrains the local topography, the drainage network, the curved fault traces, and the bended volcanic arc, which are distinct from the rest of the Andean subduction. The region's topography consists of 1000-m-high reliefs of the rocky Coastal Cordillera, which are separated from the incised rocky Precordillera (1,000–4,000 m asl) by a flat sedimentary basin known as the Central Depression (i.e., the north continuity of the Atacama Desert, Figures 1a–1c). An abrupt change in relief marks the transition between the Central Depression and the Precordillera (Figure 1b). An alignment of volcanic cones in the High Cordillera marks the geomorphological transition between the Precordillera and the 4,200 m high Altiplano (Figures 1a and 1c).

2.1.2. Lithostratigraphic Setting

The Coastal and Precordillera regions are covered by volcano-sedimentary sequences from the Mesozoic era, overlying Proterozoic to Paleozoic gneiss and granite basement (Cobbing et al. (1977); Chavez et al. (2022), see the lithostratigraphic log in Figure 1's legend and Figures 1a–1c and 1d). The base of this series is made up of Triassic to Jurassic andesites and basalts, followed by limestones and massive sandstones, and by Cretaceous volcano-clastic sequences (Alván et al., 2018; Boekhout et al., 2013; Jenks, 1948). These Mesozoic sequences have been intruded by the late Cretaceous Coastal Batholith (diorite to monzogranite, Cobbing and Pitcher (1972); Horning (1988)). The Cenozoic sequence consists of 800 m of conglomerates at its base, which were formed due to the erosion of the Andes (Bellido, 1969; Thouret et al., 2007). They are covered by volcano-clastic deposits (andesite, rhyolite, pyroclastic, ignimbrites) resulting from the activity of the Barroso Volcanic Complex (J. J. Wilson & García, 1962; Evenstar et al., 2020). Quaternary deposits consist of ignimbrites from active or recent volcanoes (Acosta et al., 2011; Wörner et al., 2000), as well as alluvial and fluvial deposits reworking these volcanic formations in valleys and the Central Depression. In addition, sparse markers of glacial erosion in higher part of the High Cordillera above 4,000 m asl can be observed (Mariño et al., 2021; Rivera et al., 2020). Massive landslide deposits also indicate fluctuating paleoclimatic conditions during the Quaternary (e.g., Caquilluco, Laguna Aricota; Zerathe et al. (2017); Zerathe et al. (2023); Delgado et al. (2020, 2022), Figures 1a and 1b).

2.1.3. Neotectonic Setting

The subduction of the Nazca plate has a convergence rate of about 60 mm/yr (Villegas-Lanza et al., 2016). As direct consequence of this active subduction, the Andean forearc displays several active fault systems.

In our study area, the Incapuquio Fault System is the primary transpressive mainly left-lateral tectonic structure that extends over more than 100 km along the Precordillera (Figures 1a and 1b). It consists of several NW-SE crustal fault segments organized in a flower structure that separates the Precordillera from the volcanic High Cordillera (Figure 1d). The core of the structure displays Paleo-proterozoic basement outcrops (Jacay et al. (2002), Figures 1a and 1d). The activity of these faults lasted since the late Cretaceous with the inversion of the Arequipa basin. More recently, microseismicity and geomorphic or paleoseismic displacement from a single M_w 7.4–7.7 earthquake in the 15th century show that the Incapuquio Fault System is active and accommodates deformation at a lithospheric scale (Benavente et al., 2017, 2021, 2022; David et al., 2005).

Among the Incapuquio segments, the Calientes fault is a 50 km-long reverse fault that separates the Precordillera reliefs from the flat plain of the Central Depression, with a 900–1,200 m-high topographic scarp (Figures 1a and 1b). The fault trace is lost to the SE at the level of the Arica Bend, which is marked by the Huaylillas Range anticline, and to the NW after the city of Sama (Hall et al. (2008), Figure 1a). The fault compressive kinematic bring the folded sedimentary and volcano-clastic Jurassic to Tertiary series in its hanging wall into contact with the Tertiary conglomerates and sediments of Quaternary alluvial fans in its footwall, indicating a post-Pliocene activity (Audin et al., 2006; Hall et al., 2008, 2012). The fault is seismically active as has produced the M_w 5 earthquake in 2005 (Tavera et al., 2007).

Finally, the 1,000 m high Coastal Range is affected by active normal faults trending perpendicularly to the subduction trench, in the continuity to the Chololo Fault System (Allmendinger et al., 2005; Audin et al., 2007, 2008).

2.2. Hydrogeological Setting of the Thermal Springs

Our study focuses on seven clusters of hot springs in the Tacna region. The local communities have been using these springs for irrigation, therapeutic and recreational purposes since time immemorial. Some of these springs and wells studied here, essentially concentrated on the geothermal field of the volcanic High Cordillera, have been previously studied by the Peruvian geological survey (Peña et al. (2009) and Cruz et al. (2010); Cruz (2018) and Cruz and Olascoaga (2021)), and are referenced in the INGEMMET's GIS (GEOCATMIN (accessed in 2022), <https://geocatmin.ingemmet.gob.pe/geocatmin/>).

The springs are found in local topographic low, that is, in valley (Figure 1b), in various geological contexts. Figure 2 presents field photographs of the emergence setting of some of these springs.

The Geisers, Barroso and Aruma springs are located in the High Cordillera at around 4,400 m asl, at the base of local volcanoes (<10 km, Figures 1a and 1b and Table 1). They are found in Quaternary volcanic rocks or in Quaternary glacial or alluvial deposits (Figures 2a and 2b).

The Ticaco and Chucatanani springs are located in the Precordillera, near the transition with the volcanic High Cordillera between 2,300 and 3,300 asl, more than 20 km away from the closest active volcanoes (Table 1, Figures 1a, 1b, and 1d). They are aligned along two different segments of the Incapuquio fault network, in Cretaceous to Paleogene crystalline rocks highly fractured due to the fault proximity (Figure 2c). Both springs are located near a contact between this intrusive rock and the Cretaceous volcano-clastic series (Figures 1a, 1c, and 1d).

The Calientes and Puquio spring clusters are aligned with the Calientes fault that marks the transition between the Central Depression and the Precordillera, between 900 and 1,300 m asl, 40–60 km away from the closest active volcanoes (Tacora and Chupiquiña, Table 1, Figures 1a, 1b and 1d). The Calientes springs are located on the fault trace, likely in its hanging wall (Figure 2d). The Calientes fault has a dip of 70°. Here the water comes out of the Quaternary conglomerate filling the Caplina canyon, which erodes the bedrocks that consists of Tertiary volcano-clastic series and Cretaceous granodiorites. Located in the damage zone of the fault, all these rocks are highly fractured and faulted. The whole is partially capped by Quaternary ignimbrites. The Puquio spring is also aligned on the Calientes fault trace, within its hanging wall (Figures 1a, 1b, and 1d). The water emerges in faulted and fractured Quaternary conglomerates eroding the Tertiary volcano-clastic series, near the tongue of the massive landslide of Caquilluco.

Finally, the wells of la Yarada are located in the Central Depression between 40 and 100 m asl, in the Quaternary alluvial plain of the Caplina River, 4–12 km away from the Pacific Ocean and 100 km away from the closest active volcano (Table 1, Figures 1a, 1b, and 1d). The Chilean springs of Colpita, Las Cuevas, Jurasse and Morales are not studied here, but shown in Figure 1a as they appear on the surface covered by the hydrothermal model.

3. Materials and Methods

3.1. Geochemical Protocols

3.1.1. Water and Gas Sampling

To ensure consistency of all our data, and supplement some missing data, we resampled some water previously studied by INGEMMET (Cruz, 2018; Cruz et al., 2010; Cruz & Olascoaga, 2021; Peña et al., 2009)) and by Vera



Figure 2. Field setting of some of the springs, and sampling locations. Abbreviations such as GEI1 correspond to sample names as described in Table 1 (a) The Geisers of Candarave (seated human for scale) and (b) the Aruma springs, both emerge in Quaternary alluvial or glacial deposits eroding Quaternary volcano-clastic rocks, (c) The Ticaco springs emerge in fractured granodiorites (floor lamp for scale), (d) The Calientes springs emerge along the Calientes fault, within the folded Quaternary (Q.) conglomerates that erode the Tertiary (T.) to Mesozoic volcano-clastic series, as well as the magmatic intrusions (car for scale). S0 is the bedding.

et al. (2021). New data have been acquired in Ticaco, Chucutamani and Puquio, following the sampling and analytic protocols detailed below.

Water and gas samples have been collected from wells, hot springs, geysers, and fumaroles in the study area. The sampling campaign occurred between the 16th and 28th of May 2022, along a transect from the coast to the volcanic High Cordillera, perpendicular to the main faults of Calientes and Incapuquio, and passing by Tacna city (Figure 1, Table 1). The water of 3 wells in La Yarada (IR24, 112, 146), 4 springs in Calientes (CAL1, 2, 3, 4), 1 spring in Puquio (PUQ1), 2 springs in Aruma (AR1, 2), 1 spring in Chucutamani (CHU1), 2 springs in Ticaco (TIC1, 2), 2 springs in Barroso (BAR1, 3) and 2 springs in Geisers (GEI1, 2) have been collected.

The water was sampled as close as possible to the emergence in order to limit degassing or evaporation effects, in favoring the highest temperature spring. Water was filtered with a 0.20 μm membrane fitted to the polypropylene syringe previously rinsed with the water from the spring. A subsample (1 ml of water) was diluted with 5 ml of 2 vol% H_2NO_3 for cation analysis, and with 5 ml UP (ultra-pure, 18.2 $\text{M}\Omega\cdot\text{cm}$) water for anion analysis. In addition, 10 ml of filtered water was also sampled for total alkalinity measurements. Aliquots of 500 ml of IR146, CAL3, PUQ1, TIC1 and GEI4 waters were sampled for isotopic analysis. Samples were stored in the fridge until analysis.

In bubbling springs (i.e., Geisers, Barroso, Aruma and Chucutamani, Figures 2a and 2b), free-gases were sampled following the water displacement method consisting to replace water by gas, when the bottle is submerged and maintained upside down, using 10- and 120-ml glass vials capped with a thick rubber septum and sealed with an aluminum collar. GEI3 was only sampled for gases. Waters for dissolved gas analysis were sampled in Barroso,

Table 1

Main Geographic and Physico-Chemical Features of the Sampled Springs and Wells Including Their Location With Respect to the Closest Volcano

Well/Spring	Sample	Locality	Sampling date	N (WGS84)	E (WGS84)	Altitude (m)	T (°C)	pH	Alkalinity (mg/L)	Closest volcano (km)	Name
IR24	IR24	La Yarada	24/05/2022	-18.191927	-70.523244	40	30	7.6	91.5	96	Tacora-Chupiquiña
IR146	IR146	La Yarada	24/05/2022	-18.175490	-70.468610	80	30	7.4	57.4	85	Tacora-Chupiquiña
IR112	IR112	La Yarada	24/05/2022	-18.149226	-70.466174	100	32	-	35.4	85	Tacora-Chupiquiña
Calientes	CAL1	Pachia	19/05/2022	-17.857287	-70.121866	1,300	42	6.9	31.7	36	Tacora-Chupiquiña
Calientes	CAL2	Pachia	19/05/2022	-17.857287	-70.121866	1,300	42	7.0	21.4	36	Tacora-Chupiquiña
Calientes	CAL3	Pachia	19/05/2022	-17.857480	-70.121728	1,300	44	7.2	40.3	36	Tacora-Chupiquiña
Calientes	CAL4	Pachia	19/05/2022	-17.857480	-70.121728	1,300	44	4.1	4.9	36	Tacora-Chupiquiña
Puquio	PUQ1	Puquio	30/05/2022	-17.773880	-70.385266	906	27	7.8	2.3	63	Tacora-Chupiquiña
Chucatamani	CHU1	Chucatamani	21/05/2022	-17.478340	-70.125704	2,310	39	7.4	56.1	33	Barroso
Ticaco	TIC1	Ticaco	20/05/2022	-17.434334	-70.038381	3,300	53	7.1	32.3	23	Barroso-Purupuruni
Ticaco	TIC2	Ticaco	20/05/2022	-17.434334	-70.038381	3,300	48	7.3	38.4	23	Barroso-Purupuruni
Aruma	AR1	Aruma	26/05/2022	-17.702694	-69.835895	4,470	45	<2.0	-	8	Tacora-Chupiquiña
Aruma	AR2	Aruma	26/05/2022	-17.702694	-69.835895	4,460	64	2.2	-	8	Tacora-Chupiquiña
Barroso	BAR1	Barroso	23/05/2022	-17.388730	-69.764021	4,420	50	7.8	187.9	10	Barroso
Barroso	BAR3	Barroso	23/05/2022	-17.390050	-69.765212	4,440	84	8.0	5.5	10	Barroso
Geisers	GEI1	Candarave	22/05/2022	-17.102773	-70.133247	4,390	73	7.8	99.5	11	Yucamane
Geisers	GEI2	Candarave	22/05/2022	-17.102773	-70.133247	4,390	87	5.0	0.2	11	Yucamane
Geisers	GEI3	Candarave	22/05/2022	-17.102773	-70.133247	4,388	42	5.0	-	11	Yucamane
Geisers	GEI4	Candarave	22/05/2022	-17.102773	-70.133247	4,388	-	-	-	11	Yucamane

Aruma, Ticaco, Chucatamani, Calientes and in the IR146 and IR112 wells of la Yarada by fully filling glass vials (40-, 60-, and 120-ml) to the top to prevent air contamination and sealing them while still underwater with a thick rubber septum secured with an aluminum collar.

3.1.2. Geochemical Analysis

Water analysis has been performed using the Geochemistry-Mineralogy platform of ISTerre (OSUG-France) between September 2022 and January 2023. Cations have been analyzed with a Varian 720-ES ICP-AES. Anions were analyzed with a Dionex Integrion™ Ionic Chromatograph. Total alkalinity was measured by a Gran titration (Dickson, 1981). All ionic concentrations are given with a precision of 5% at the 95% confidence level (precision and accuracy values are reported in Table S1 in Supporting Information S2). Among the 16 water samples analyzed only 4 samples (IR-24, AR1, AR2, and GEI2) display ionic balances >10% (see Table S1 in Supporting Information S2). The “Diagrammes” software (Simler, 2014) was used to calculate the Total Dissolved Solids (TDS) and draw the Piper and ternary diagrams.

The water stable isotopes δD and $\delta^{18}O$, carbon isotopes $\delta^{13}C$ and radiocarbon ages were measured by the Beta Analytic® laboratory (Miami, USA). The water stable isotopes δD and $\delta^{18}O$ were measured using a gas-bench Isotope Ratio Mass Spectrometer (IRMS). Radiocarbon ages are reported as Radiocarbon Years Before Present = AD 1950 issued from the measurement of the carbon isotopes $\delta^{13}C$ measured using an Accelerator Mass Spectrometry (AMS). All values are given in Table S2 in Supporting Information S2.

Gas analysis were carried out at the ISTerre laboratory (Grenoble) with a Perkin Elmer® CLARUS 500 Gas Chromatograph (GC) equipped with a thermal conductivity detector and a 2 m long column (RESTEK® Shin Carbon ST 80/100) with Ar as a carrier gas. The GC was calibrated using several Ar, O₂, N₂, H₂, CH₄, CO₂ gas mixtures. The estimated analytical error is estimated at ±3% within the 97% confidence level. The obtained free gas concentration values have been corrected for air contamination assuming all measured O₂ comes from air. For the dissolved gases, a known volume of water was extracted and simultaneously replaced by Ar. The vials were then agitated to allow degassing of the fluid for 48 hr. The gas headspace was then sampled and analyzed by GC.

Dissolved gas concentration was calculated using the Henry law, and the PHREEQC software (Parkhurst & Appelo, 1999) for dissolved carbonate speciation, accounting for the water pH and salinity. Tap water is also analyzed for comparison with water equilibrated with air.

3.1.3. Estimation of the Recharge Elevation and Geothermometers

The hydrogen and oxygen isotope contents of rainwater decrease as altitude increases (Ambach et al., 1968). The altitude at which groundwater has been infiltrated can be approximated by using calibration curves of the isotopic ratio of local meteoric water, because no further fractionation occurs after precipitation. The water stable isotope $\delta^{18}\text{O}$ is used to calculate the elevation of the water recharge. Because of the absence of continuous sampling transects within the Andes and the complex climatic and orogenic effects, the local $\delta^{18}\text{O}$ gradient is not clearly defined, being subject to semi-monthly to interannual timescale variations (P. G. Aron et al., 2021). To evaluate the fluid recharge elevations, we utilized various regional gradients issued from the literature: $-4.3 \pm 1.8 \text{‰/km}$ in the region of Moquegua (-17°S , 100 km north of the study region, P. G. Aron et al. (2021)); $-4.1 \pm 1.0 \text{‰/km}$ in the region of Arica (-18°S , 50 km south of the study area, data from Sánchez-Murillo et al. (2018) in the Waterisotopes Database (Putman and Bowen (2019), accessed 14/02/2023); and finally, the mean gradient modeled by Insel et al. (2012) for the 18°S : $2.8 \pm 0.8 \text{‰/km}$. Considering these uncertainties we discuss the large zones suggested by the estimations rather than the absolute values.

Traditional geothermometers reflect temperatures of chemical equilibration between the fluid and the surrounding rocks at depth. Geothermometers are based on theoretical or empirical relations that use ionic concentrations to estimate temperature. It is assumed that the water-rock thermodynamic equilibrium is achieved and preserved during fluid ascent (Cioni & Marini, 2020; White, 1965). Given the uncertainties about this context in the study area, various traditional geothermometers, that is, quartz (R. O. Fournier, 1973; R. Fournier & Potter, 1982), chalcedony (R. O. Fournier (1973); Arnórsson et al. (1983), Na-K (Arnórsson et al., 1983; Santoyo & Díaz-González, 2010), $\text{Na}^2\text{-Ca}$ (Arnórsson et al., 1983; Santoyo & Díaz-González, 2010) and $\text{K}^2\text{-Ca}$ (Arnórsson et al., 1983; Santoyo & Díaz-González, 2010), have been calculated in order to compare the general trends of reservoir temperatures for each spring.

3.2. Numerical Modeling

Hydrothermal processes have been explored in a 3D model constructed from a true topography and a simplified structural model accounting for a homogeneous volume of host-rocks intersected by regional faults. Rocks are considered as porous and permeable medium because the primary influence on fault and host rock permeability is fracture density. This assumption enables the specific coupling of the Darcy law and heat transfer equations in the COMSOL MultiphysicsTM5.2 software. Governing equations are given in Appendix A.

3.2.1. Geometry and Mesh

The area considered in the model has a regional scale that corresponds to the map in Figure 1a, which is 157 km long (E-W) and 140 km wide (N-S, Figure 3). This area encompasses all the studied hot springs and wells, and an additional distance from the springs in order to prevent boundary effects (Figure 1). The upper surface of the model corresponds to the true topography of an issued 30m-ALOS (Advanced Land Observing Satellite, https://www.eorc.jaxa.jp/ALOS/en/dataset/aw3d30/aw3d30_e.htm) Digital Elevation Model degraded by interpolation into a 2 km resolution in order to facilitate the geometry construction and reduce the computation time. The highest point of the topography corresponds to the Tacora volcano (5,782 m asl). The base of the geometry is fixed at $-2,500$ m below the mean sea level, in order to guarantee temperature and pressure conditions where water remains in a liquid state. In crystalline rocks aquifers, the position of the water table in relation to the topography may be disregarded as it has little influence on the regional flows (Gleeson & Manning, 2008). For the sake of simplicity we consider full saturation so that this interpolated topographic surface corresponds to the water table.

Three faults are included in the model: two segments of the Incaquiquio fault system (North and South) and the Calientes fault (Figure 3). As we lack knowledge of the faults' geometry at depth, we can only rely on the dips of the fault observed on the surface and of nodal planes of focal mechanisms at the regional scale (Gaidzik & Wiesek, 2021). To preserve the suspected flower-like structure at the section scale (Figure 1d), the northern segment of the Incaquiquio fault dips of 70° to the South (Benavente et al., 2017), the southern segment of the Incaquiquio fault is vertical, and the Calientes fault dips 70° to the North (field observation, Figure 2d, see Table

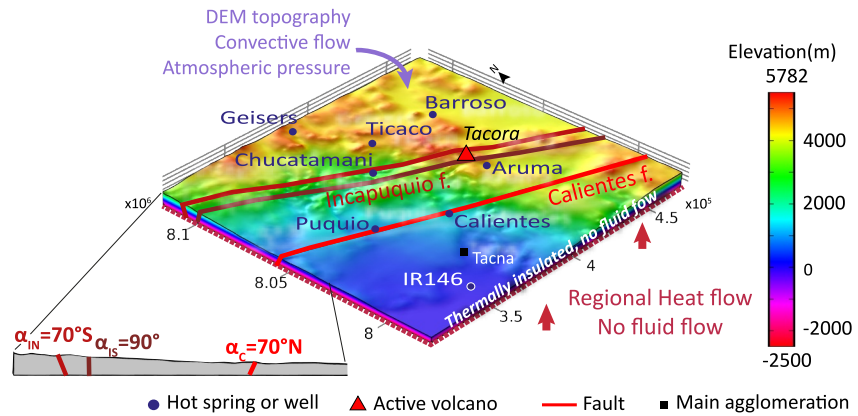


Figure 3. 3D geometry and boundaries conditions of the numerical hydrothermal model. α_C , α_{IN} and α_{IS} correspond to dip of Calientes faults and Incapuquio North and South faults, respectively. DEM = Digital Elevation Model.

2). Faults are simulated as planar surfaces that extend from the base of the simulated block to its surface. Faults are not connected to each other and therefore separate the model into four compartments. A sensitivity study is carried out on the thickness of the fault zone d (m), in an interval 50–1,500 m corresponding to the expected values for regional faults (Savage & Brodsky, 2011, Table 2). In the damage zone, the permeability will differ from those in the host rock compartments.

A mesh convergence study was performed by refining the mesh until a solution similar to the previous one (within a maximum difference of 1°C) was found. A polygonal mesh grid of 171,518 elements has accordingly been built over the entire geometry. The mesh is refined around the topographic complexities, and the fault planes. The mean element size is 3,527 m in the main volume and 2,600 m in the faults.

Table 2

Parameters of the Hydrothermal Numerical Model, ^(a) Function of the Temperature, ^(b) Depending on the Model Compartment (Host-Rock, Fault Zone, See the Main Text)

Model properties			
Fault dip	α	70/90	°
Fault thickness	d	50–1,500	m
Basal heat flow	Q_0	0.12	W/m ²
Geothermal gradient	ΔT	50	°C/km
Coefficient of heat transfer	h	0.025	W/(m ² .K)
Fluid properties			
Dynamic viscosity	μ	f(T) ^a	Pa.S
Thermal conductivity	λ_f	0.6	W/(m.K)
Thermal capacity	Cp_f	4,180	J/(kg.K)
Mass density	ρ_f	f(T) ^a	kg/m ³
Rock properties			
Porosity	Φ	0.1	
Thermal conductivity	λ_r	2.5	W/(m.K)
Thermal capacity	Cp_r	1,000	J/(kg.K)
Mass density	ρ_m	2,650	kg/m ³
Permeability	k	Variable ^b	m ²
Maximum permeability at the surface	k_{b0}	10^{-16}	m ²
Permeability decreasing with depth	δ	2,500	m

3.2.2. Equations of State

The heat transfer equation and Darcy's law are coupled by the fluid velocity in the governing equation (see Appendix A). Coupling is also ensured by the equations of state applied to the fluid. For the conditions of pressure (0.05–75 MPa) and temperatures (0–375°C) calculated in this study, the water remains in the liquid state (see Figure S1 in Supporting Information S1). Under these conditions, fluid density and viscosity vary essentially as a function of temperature T (°C), and pressure and salinity are negligible (Jupp & Schultz, 2004; Potter & Brown, 1977). As used in Rabinowicz et al. (1998), the fluid viscosity μ (Pa.s) and the fluid density ρ_f (kg/m³) vary in the range of 0–400°C such as:

$$\mu(T) = 2.414 \times 10^{-5} \cdot \exp\left(\frac{247.8}{T + 133}\right) \quad (1)$$

and

$$\rho_f(T) = 1036.5 - 0.14167 \cdot T - 0.0022381 \cdot T^2 \quad (2)$$

3.2.3. Model Parameters

Parameters of the model and specifically the fluid and rock properties are given in Table 2. Permeability is the only parameter that differs between host rock and faults. It is a poorly constrained property, with values that can vary over several orders of magnitude. Although lateral lithological variations have been observed in the field (Figures 1 and 2), we

consider in this first version of the model that the permeability of the whole host rock k_{hr} (m^2) is homogeneous, decreasing with depth z (m) such as:

$$k_{hr} = k_{b0} \cdot \exp\left(\frac{z - 800}{\delta}\right) \quad (3)$$

with k_{b0} (m^2) being the maximum permeability at the surface (taken here as $10^{-16} m^2$) and δ (m) defining the decrease in permeability with depth, taken at $-2,500$ m (Duwiquet et al., 2021).

The activity of the Incapuquio and Calientes faults is expected to increase the host-rock permeability in unknown proportions. A sensitivity analysis has been conducted on the fault permeability k_f being homogeneous with values between 10^{-16} and $4 \times 10^{-13} m^2$ (Evans et al., 1997; Sonney & Vuataz, 2009).

3.2.4. Boundary and Initial Conditions

3.2.4.1. Flow Conditions

An elevation-dependent atmospheric pressure $P_{atm}(z)$, from the International Civil Aviation Organization Standard Atmosphere (ICAO, 1993), is imposed on the topographic surface (Figure 3), such as:

$$P_{atm} = P_0 \cdot \left(1 - \frac{0.006 \cdot z}{288.15}\right)^{5.255} \quad (4)$$

where $P_0 = 10^5$ Pa is the atmospheric pressure at sea level and where z (m) is the elevation. Below the surface, a hydrostatic pressure gradient $\rho \cdot g$ is added to P_0 . No flow is allowed through the lateral limits of the model.

3.2.4.2. Thermal Conditions

Because of the lack of local heat flow data, a constant heat flow value of $Q_0 = 0.12$ W/m² determined by Hamza et al. (2005) is applied at the base of the geometry (Table 2). Similarly, a regional geothermal gradient $\Delta T = 50^\circ\text{C}/\text{km}$ is maintained for the entire block (Vieira & Hamza, 2019). Potential magmatic chambers are not replaced.

In order to allow for temperature variations at the surface (cold areas at high altitudes but also warm zones where hot springs emerge), a mixed thermal boundary condition like that used in Magri et al. (2016) and in Taillefer et al. (2018), is applied to the topographic surface:

$$Q = h(T_s - T) \quad (5)$$

where Q (W/m²) is the surface heat flow, h (W/(m².K)) a coefficient of heat transfer and T_s ($^\circ\text{C}$) the reference temperature at the surface, that corresponds to the regional atmospheric temperature gradient determined from local data (National Oceanic and Atmospheric Administration, NOAA (2022)):

$$T_s = 20 - 0.030 \cdot z \quad (6)$$

A h value of 0.025 W/(m².K) has therefore been calibrated following the method described by Taillefer et al. (2018) that combines a recharge temperature between 0 and 20°C and a discharge at the surface.

The initial conditions are a hydrostatic pressure and a purely conductive thermal state, from which a steady state is computed.

4. Results

4.1. Composition of Springs Waters and Gases

4.1.1. Water Physico-Chemistry

Spring temperatures range between 27°C (Puquio) to 87°C (Geisers, Figure 1, Table 1). The highest temperatures (84 – 87°C) are recorded at Barroso and Geisers springs. The Aruma springs show mid-hydrothermal temperatures between 45 and 64°C . Hot springs in the Precordillera have low to moderate temperatures between 27 and 53°C

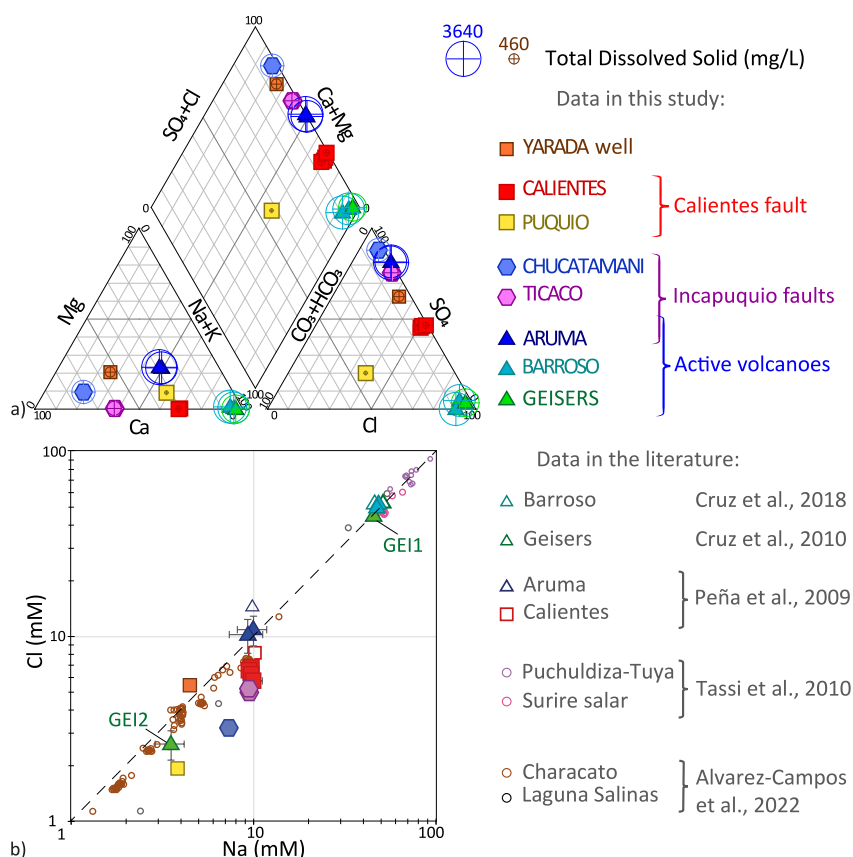


Figure 4. Composition in major ions of the thermal water. (a) Piper diagram (Piper, 1944). Colored circles represent the water Total Dissolved Solids (TDS, mg/L) and are proportional to the circles, and in the legend, (b) Na-Cl diagram (Log-log) with data from previous studies (Cruz, 2018; Cruz et al., 2010; Peña et al., 2009) and of near hydrothermal systems in the region (Alvarez-Campos et al., 2022; Tassi et al., 2010). Dotted line corresponds to $Na/Cl = 1$. Complete data is available in Table S1 in Supporting Information S2 and in Taillefer et al. (2024).

(Puquio, Calientes, Chucutamani, Ticaco). The temperatures of water flowing out of the wells in the Yarada in the Central Depression (IR24, 112 and 146) are between 30 and 32°C. The pH of most of the springs is close to neutrality, except for the Geisers-GEI2 (pH = 5) and the Aruma springs (pH = 2).

Springs located close to active volcanoes have high TDS above 2,980 mg/L compared to the other springs and wells that are between 460 and 2,460 mg/L (Figure 4a). Barroso and Geisers are Na-K-Cl waters with similar compositions. Chucutamani and Ticaco are Ca-SO₄ waters, as well as the IR146 well in la Yarada. The Aruma, Calientes and Puquio springs have Na and K as dominant cations, which is an intermediate composition between the Barroso and Geisers springs and the other waters. Dominant anions are sulfates (80%) in Aruma, sulfates and chlorides (50% each) in Calientes and carbonates and chlorides in Puquio (40% each).

Most of the springs have Na/Cl ratio >1 , unless GEI2, Barroso, Aruma and IR146 that have Na/Cl ratio ≤ 1 (Figure 4b). The Barroso and Geisers springs have Na and Cl concentrations around 50 mM (except GEI2) while the other springs show concentrations ranging from 2 to 11 mM (see Table S1 in Supporting Information S2).

Finally, one may also note that Aruma springs have high concentrations of Fe, Al, Mn, Zn, while the Barroso and Geisers springs display high Li and B concentrations (Table S1 in Supporting Information S2). The complete geochemical data set is available in Taillefer et al. (2024).

4.1.2. Gas Composition

Free gases from Geisers and Barroso springs are composed of more than 90 vol% CO₂, except for GEI3 (70 vol% CH₄, Figure 5a). The free gas bubbling in the Chucutamani spring is mostly composed of N₂ (>95 vol%). The

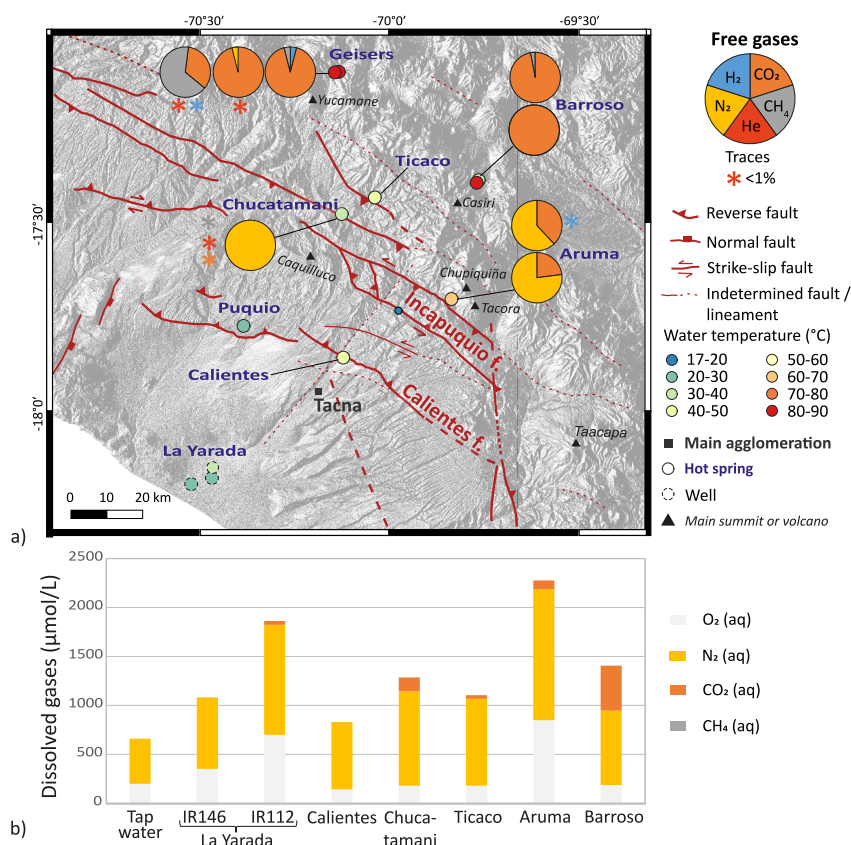


Figure 5. Gaseous composition of the thermal waters. (a) Free gases in proportion of total gases, (b) Dissolved gases concentrations in proportion of total gases. Complete data in Tables S3 and S4 in Supporting Information S2.

spring of Aruma has a mixed composition of N₂ (60–80 vol%) and CO₂ (20–40 vol%). Traces of He are detected in the springs of Geisers and Chucutamani (20–200 ppmv), and traces of H₂ are found in Geisers, Ticaco and Aruma (10–300 ppmv). Complete data is given in Table S2 in Supporting Information S2.

The concentration of dissolved N₂ appears to be significantly higher than that of an equilibrated water with air (e.g., tap water, 460 μmol/L) in all the water samples (Figure 5a), except for IR146, IR112 and Aruma, which show significant air contamination (see Table S3 in Supporting Information S2 for more details). Specifically, dissolved N₂ in excess is the sole gaseous constituent detected in the Calientes spring (688 μmol/L). The Barroso water displays a proportionally higher concentration of dissolved CO₂ (456 μmol/L) than the other springs containing this gas (37–142 μmol/L). Traces of CH₄ are detected in Ticaco and Barroso (1–4 μmol/L).

4.1.3. Isotopic Data of the Waters

The Calientes and Ticaco springs, as well as the Yarada well, plot on the Global Meteoric Water Line (Craig, 1961) and on the Local Meteoric Water Line (Boschetti et al. (2019), Figure 6). The Geisers spring has isotopic values that fall on the Local Mixing Line, which connects isotopic values of local meteoric water (Cortecci et al., 2005) with the isotopic values that characterize the andesite (i.e., subduction arc) water pole (Fischer & Chiodini, 2015; Sakai & Matsubaya, 1977). The complete isotopic data set is available in Table S4 in Supporting Information S2.

4.1.4. Infiltration Elevation and Radiocarbon Ages

The current water of the IR146 well of la Yarada and of Ticaco and Geisers springs is characterized by similar δ¹⁸O isotopic values between −12.4 and −12.6 ‰ (Table S4 in Supporting Information S2), resulting in identical recharge elevations between 2,890 and 4,670 m asl, at the transition zone between the Precordillera and the volcanic High Cordillera (Figure 6b). The Calientes and Puquio springs have close δ¹⁸O isotopic composition

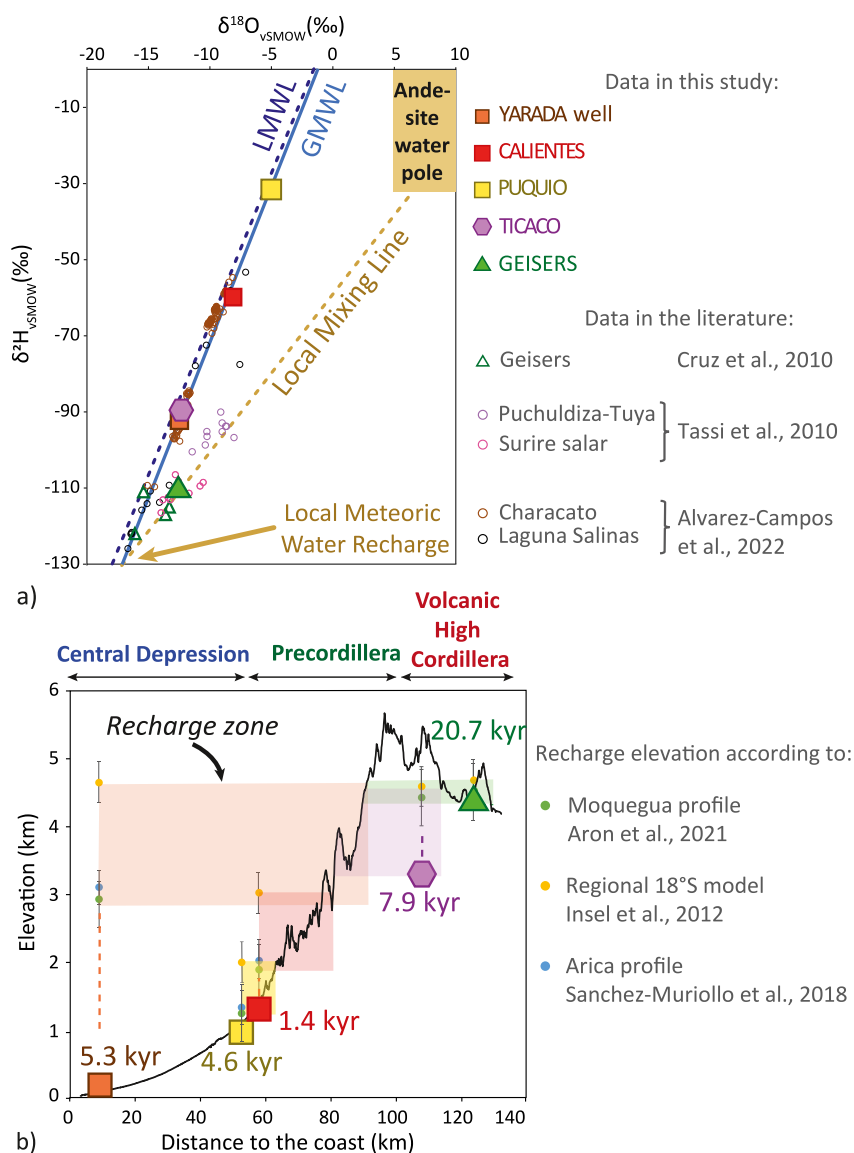


Figure 6. Isotopic composition of the thermal waters. (a) $\delta^{18}\text{O}$ versus $\delta^2\text{H}$ diagram with the Global Meteoric Water Line (GMWL, Craig (1961)), the Local Meteoric Water Line (LMWL, Boschetti et al. (2019)), and the Local Mixing Line linking the Local Meteoric Water Recharge (Cortecchi et al., 2005; Cruz et al., 2010) with and the Andesite (i.e., subduction arc) Water Pole (Fischer & Chiodini, 2015; Sakai & Matsubaya, 1977). Additional data on other springs nearby (Alvarez-Campos et al., 2022; Cruz et al., 2010; Tassi et al., 2010) are also represented. (b) Topographic profile between the Ocean level to the High Cordillera with the location of the springs and wells, their radiocarbon ages in kyrs and the elevation of their recharge zone calculated after Insel et al. (2012), Sánchez-Murillo et al. (2018) and P. G. Aron et al. (2021) (colored dots). The complete data set is available in Table S2 in Supporting Information S2.

(−8.1 and −5.0 ‰, respectively, see Table S4 in Supporting Information S2) resulting in close recharge elevations between 1,260 and 3,000 m asl, at the transition zone between the Central Depression and the Precordillera.

The IR146 well of la Yarada and the Puquio springs show close apparent ages of $5,270 \pm 20$ years and $4,590 \pm 20$ years, respectively (Table S4 in Supporting Information S2). The Ticaco spring also has an apparent age in the same order of magnitude ($7,880 \pm 20$ years). The water of the Calientes spring has the youngest apparent age of $1,370 \pm 30$ years. The water of the Geisers spring is the oldest ($20,670 \pm 60$ years).

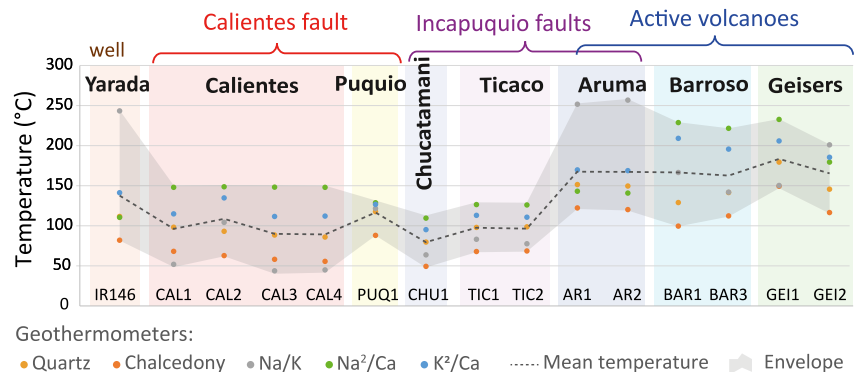


Figure 7. Reservoir temperature according to various classical geothermometers (dots, see Section 3.1.3 and Table S5 in Supporting Information S2 for details about the methodology). The mean of temperatures (dot line) and the envelope between the maximum and minimum values (gray surface) shows the general trend.

4.1.5. Reservoir Temperature

The envelope between the minimum and maximum reservoir temperature estimated for each spring shows the general trends: hot springs close to active volcanoes (Aruma, Barroso, Geisers) are characterized by the hottest reservoir temperatures, with a mean at 170°C Figure 7. Hot springs located along faults show similar trends, with a mean of 90°C for those located on the Incapuquio fault segments, and a mean of 100°C for those located on the Calientes fault. The reservoir temperature of the well in la Yarada IR146 is significantly higher than the fault-related springs, with a mean of 140°C.

4.2. Hydrothermal Numerical Model

Field data, and in particular geochemical analysis of the hydrothermal fluids, provide information about the temperatures, compositions and origin of the different hydrothermal springs and their location with respect to the volcanoes, the forearc faults and the topography. In order to decipher the relative contributions of these elements on fluid circulation and heating, hydrothermal numerical modeling appears as a complementary and exploratory tool.

4.2.1. Preliminary Study of the Thermal Regime: The Critical Rayleigh Number and Permeability

In the numerical model, fluid flow can be driven by topography (i.e., forced convection) and/or by buoyancy (i.e., free convection). An analysis of the Rayleigh number Ra and the calculation of the critical permeability k_c from which the free-convection occurs enable to designate the dominant thermal regime in the basement and the faults (e.g., Magri et al. (2016)). Equations are given in Appendix B.

The value of ρ_f is taken at the minimum temperature (here 0°C) and calculated from Equation 2 resulting in $D_\lambda \sim 5.3 \times 10^{-7} \text{ m}^2/\text{s}$. Considering (a) a basement thickness of 8,300 m between the highest elevation (5,800 m) and the base of model (-2,500 m), (b) an average permeability of the host-rock $k_{hr} = 4 \times 10^{-17} \text{ m}^2$, (c) a difference of temperature $\Delta T = 284^\circ\text{C}$ between the top (mean of 16°C) and the base (mean of 300°C) of the model, and (d) fluid and rocks properties as indicated in Table 1, the computed Rayleigh number for the basement is $Ra \sim 0.16$. This value is smaller than $4\pi^2$, the critical Rayleigh number Ra_c from which free convection is likely to start. This means that the thermal regime in the basement is only driven by the topography (forced convection).

For the Calientes fault, assuming a fault thickness $d = 100 \text{ m}$, and a mean fault height $H_C = 5,100 \text{ m}$, the critical Rayleigh number $Ra_{cf}/4 = 167$ and the inferred critical permeability for which thermal convection may occur in the fault is thus $k_{cf,C} = 3 \times 10^{-14} \text{ m}^2$. For the Incapuquio faults, assuming a mean fault height $H_I = 6,300 \text{ m}$, the critical Rayleigh number $Ra_{cf}/4 = 206$, and the critical permeability $k_{cf,I} = 4 \times 10^{-14} \text{ m}^2$. Free convection is likely to occur in the computed model at fault permeability higher than these close critical values.

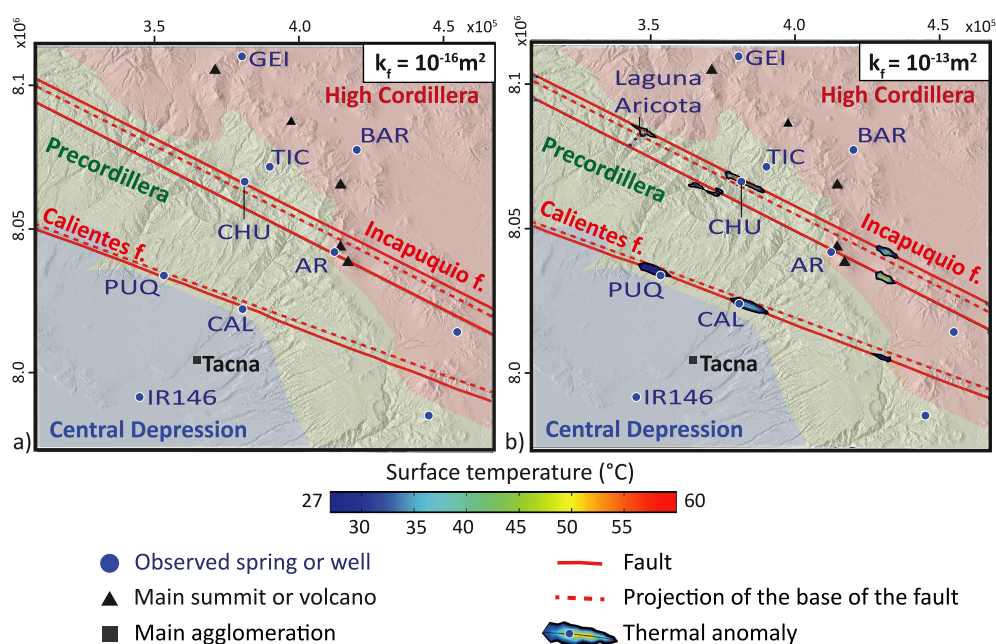


Figure 8. Thermal anomalies on the topographic surface of the numerical model, (a) for poorly permeable faults $k_f = 10^{-16} \text{ m}^2$, (b) for highly permeable faults $k_f = 10^{-13} \text{ m}^2$. The fault thickness $d = 100 \text{ m}$.

4.2.2. Surface Temperatures Versus Fault Permeability

Increasing fault zone permeability can cause thermal anomalies to appear on the surface of the model (Figure 8). For low fault permeability ($k_f = 10^{-16} \text{ m}^2$), no thermal anomaly is visible on the surface (Figure 8a). However, when fault permeability is elevated ($k_f = 10^{-13} \text{ m}^2$), patches of convective warm flows appear on the surface along the fault planes, which correspond to the location of (a) the Calientes and Puquio springs along the Calientes fault, and (b) the Chucatamani spring and the Laguna Aricota lake along the Incapuquio fault (Figure 8b). The location of thermal anomalies remains constant regardless of permeability (for values higher than $k_f = 1 \times 10^{-14} \text{ m}^2$). No anomaly is observed for the other springs, including the Aruma spring, although it is located along the Incapuquio faults. Patches on the Incapuquio faults extremities are due to boundaries effects.

4.2.3. Fluid Circulation

These thermal anomalies generated at the surface mainly result from circulations along the fault planes when the faults are permeable, and to a lesser extent, from circulations in the basement (Figure 9). The flow lines that contribute to the Puquio and Calientes thermal anomalies mainly originate from the intersection between the Calientes fault and the Precordillera reliefs at the Arica Bend (i.e., the Huayllillas Range watershed, Figure 9a). They follow the fault plane at depth where they heat and then contribute to the thermal anomalies of Calientes or Puquio. A large part of these flow lines also leaves the Calientes fault toward the Ocean, passing beneath the Tacna city and near the la Yarada wells (IR146). Warm flow lines up to 275°C that circulate in the basement contribute in a smaller proportion, to the thermal anomalies. They originate from the Tacora-Chupiquiña volcanoes for Calientes and from the Caquilluco watershed for Puquio. The flow lines supplying the Chucatamani thermal anomaly mainly originate from the High Cordillera (i.e., the Barroso and Purupuruni watersheds) and circulate along the North Incapuquio fault and in the basement, passing through the location of Ticaco (Figure 9b). Some of these flow lines also leave the Incapuquio faults at depths toward the ocean, in the direction of the Calientes and the Puquio springs.

4.2.4. Heat Anomalies Along the Fault

The detailed observation of the fluid circulation along the fault planes for high fault permeability ($k_f = 10^{-13} \text{ m}^2$) reveals the alternating of hot and cold fluid plumes with wavelengths of 30–50 km (Figure 10). At the intersection of the Calientes fault and the Precordillera at the Arica Bend (see Figures 1a and 1b), there is a significant recharge

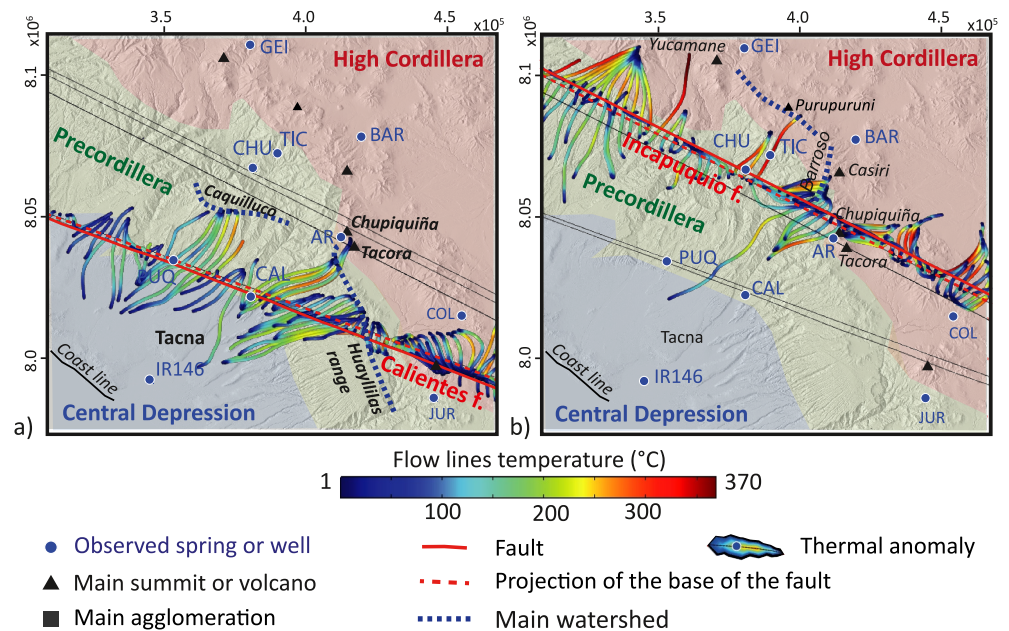


Figure 9. Flow line temperatures and surface anomalies (also see Figure 8) for a fault permeability $k_f = 10^{-13} \text{ m}^2$ and a fault thickness $d = 100 \text{ m}$. Flow lines contributing to (a) the Calientes fault and (b) the North Incapuquio fault.

zone of cold fluids (minimum 5°C , Figure 10a). Moving northward, two hot plumes appear beneath the location of the Calientes and Puquio springs, separated by a small recharge zone. The highest Darcy velocities (up to $1.13 \times 10^{-7} \text{ m/s}$) are located where the faults meet the steepest topographic gradients (Figure 10b). Infiltrated fluids are driven toward the northwest and are heated up to $100\text{--}250^\circ\text{C}$ before reaching the surface beneath the Calientes and Puquio springs. Flow lines depicted in Figure 10b suggest that fluids originating from the NW may also contribute to the Puquio spring, albeit to a lesser extent and at lower temperatures (up to 170°C).

A nearly identical pattern is observed along the Incapuquio fault, where cold fluids infiltrate massively at the fault intersection with the High Cordillera (Figure 10c). The location of the Aruma spring corresponds to this

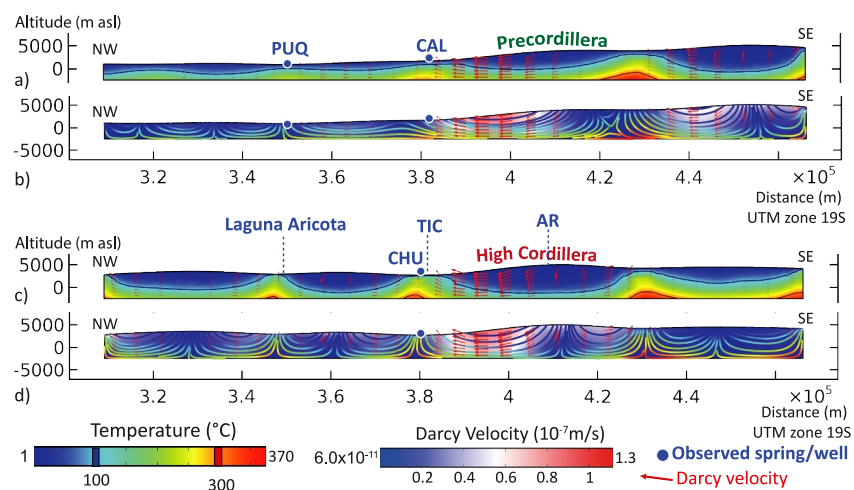


Figure 10. Heat anomalies and Darcy velocities along the Calientes and the North Incapuquio fault planes for fault permeability $k_f = 10^{-13} \text{ m}^2$ and thickness $d = 100 \text{ m}$. PUQ = Puquio, CAL = Calientes, CHU = Chucutamani, TIC = Ticaco and AR = Aruma. (a) Temperatures, isotherms and orientation of the Darcy velocities along the Calientes fault, (b) Darcy velocities and flow lines colored according to the temperature along the Calientes fault, (c) Temperatures, isotherms and orientation of the Darcy velocities along the North Incapuquio fault, (d) Darcy velocities and flow lines colored according to the temperature along the North Incapuquio fault.

infiltration zone. Moving northward, two hot plumes can be observed below the Chucutamani and Ticaco springs, as well as the Laguna Aricota (see Figure 8b). Unlike the Calientes fault (Figure 10a), these two plumes are separated by a significant infiltration zone. Similar to the Calientes fault, high Darcy velocities correspond to the steepest topographic gradient, allowing infiltrated fluids to flow toward the Chucutamani and Ticaco sources, reaching temperatures up to 170°C (Figure 10d). A contribution of fluid from the northwest is possible to a lesser extent.

Plumes are also observed along the Calientes and Incapuquio fault planes on the Chilean side of the frontier at 340,000 longitude. The faults' continuity in this direction is unclear, so although interesting, they are not interpreted in this study. Plumes located at the boundaries of the model are due to boundary effects.

5. Discussion

In the following sections, the geochemical composition of the hydrothermal fluids is discussed to determine how they are related to each other and to which type of hydrothermal system (volcanic or orogenic) they belong. This analysis allows us to decipher what are the main sources of heat and the main fluid pathways associated with each spring.

5.1. The Volcanic Field Hydrothermal Systems

Geisers and Barroso springs, spatially located on the volcanic High Cordillera, are characterized by similar geochemical features: high TDS, high temperatures of both their respective emergence (Table 1) and reservoir (Figure 7), a Na-K-Cl dominated composition with Na/Cl = 1 (Figure 4), anomalies of Li and B (Table S1 in Supporting Information S2), and free-gas dominated by CO₂ (Figure 5). These results, consistent with those of Cruz et al. (2010) and Cruz (2018) (Figure 4), are typical of closed hydrothermal systems associated with magmatic heat sources. This magmatic contribution is necessary to produce elevated temperatures (Table 1 and Figure 7), fluid-rock interactions resulting in a salted composition (Figure 4b), and mixed isotopic composition between the meteoric and andesitic water poles (Figure 6). All of these parameters allow categorizing these springs in the volcanic hydrothermal types as defined by Moeck (2014).

5.2. The Orogenic Belt Hydrothermal Systems

In contrast, the Puquio, Calientes, Chucutamani and Ticaco springs share similar features, the first being their location along major faults 20–60 km away from volcanoes (Table 1). They also have low to moderate TDS, moderate temperatures of both their emergence and reservoir (Table 1 and Figure 7), and Na/Cl ≤ 1 (note that our data set is consistent with those of Peña et al. (2009), see Figure 4b). Additionally, gas composition is dominated by N₂ (Figure 5). Both the water composition and isotopic signature, which is purely meteoric, align with the features described by Alvarez-Campos et al. (2022) in a nearby non-volcanic hydrothermal system (Figures 4b and 6). These authors provide evidence that local salars and mountain rocks constitute the main origin of the fluids, without magmatic contribution. Based on these parameters, these springs can be classified as belonging to the “orogenic belt” hydrothermal types (Moeck, 2014).

In more details, we differentiate two subgroups:

The springs of Ticaco and Chucutamani, both located on the North Incapuquio fault, share similar Ca-SO₄ dominated composition (Figure 4), suggesting a common origins and histories of fluid-rock interactions. The similar geological setting of these springs (Figures 1a and 1d), the high altitude of recharge indicated by water isotopes (Figure 6b), and flow lines in numerical models (Figures 9b and 10d), all agree in favor of a fluid origin in the High Cordillera and a common fluid migration in the fractured crystalline rocks near the Incapuquio fault (Figure 2c).

The Calientes and Puquio springs, both located on the Calientes fault, have similar compositions but differ in their CO₃-HCO₃ content and salinity (Figure 4a), their temperatures (Figures 1 and 7) and their water age (Figure 6). This suggests a partially shared history. As shown by the isotopic composition (Figure 6) and numerical model (Figures 9a and 10a and 10b), fluids infiltrate at moderate altitudes in the Precordillera, and then circulate along the Calientes fault. The oldest age and highest reservoir temperature at Puquio could be explained by a more extended and deeper hydrothermal loop from the main recharge zone, as shown in Figure 10b. In contrast, the low

temperature, salinity and $\text{CO}_3\text{-HCO}_3$ -rich composition of the Puquío spring suggest a probable contribution from shallow groundwater (Giggenbach, 1988), which could originate from the Northwest (Figure 10b).

Finally, the wells of la Yarada share many similarities with the springs related to the Incapuquío faults, including identical chemical and isotopic compositions (Figures 4 and 6a), supporting a common origin. As suggested by isotopic composition (Figure 6b) and the flow lines in the model (Figure 9), the fluids could originate from the limit between the High Cordillera and the Precordillera, likely in a geological setting close from the Ticaco and Chucutamani springs. This presupposes that the faults are sufficiently permeable to allow these fluids to cross them toward La Yarada. Fluids reach reservoir temperatures significantly higher than the forearc springs (Figure 7) since they have been driven to greater depths under the effect of the substantial topographic gradient between the recharge zone and the wells (Figure 6b). The low temperature (Table 1) and the $\text{Na/Cl} > 1$ of the well water (Figure 4b) could be explained by mixing with surface water, such as seawater from marine intrusion (Chucuya et al., 2022; Vera et al., 2021).

5.3. The Mixed Hydrothermal Systems

The Aruma springs, located near the active volcanoes and on the Incapuquío fault, are characterized by geochemical features belonging to both volcanic and orogenic systems. The presence of a mixed hydrothermal system is supported by the composition of the free gas phase, which contains a mixture of CO_2 and N_2 (Figure 5), like in similar contexts in the volcanic Western Cordillera in Bolivia (Moretti et al., 2023). On one hand, the particularly low pH, the elevated TDS and temperatures of both emergence and reservoir (Table 1 and Figure 7), and $\text{Na/Cl} = 1$ (Figure 4b), are characteristic of volcanic hydrothermal systems. This is further supported by the inability to replicate the temperature of the Aruma springs, which are located on a major cold recharge zone in numerical model (Figure 8a). In considering the contribution of a magmatic heat source, the hydrothermal loop between the recharge zones to the springs should be short and peripheral to the volcanic edifices (in the “outflow zone,” Hochstein (1988), e.g., Byrdina et al. (2013)). On the other hand, the composition of the Aruma spring differs significantly from that of the other volcanic springs but is similar to that of the Chucutamani and Ticaco springs (Figure 4). This indicates a likely connection between these fluids along the Incapuquío fault, as shown by flow lines in the numerical model (Figure 10d).

In this section we have observed that the geochemistry of the different hydrothermal systems is influenced by the origin of the fluids and by the pathways they follow within the host rocks and along the faults. The following sections explore in detail these two aspects of the hydrothermal loop.

5.4. Fluid Recharge and Origin

Since most of the hydrothermal fluids in the Tacna region are of meteoric origin (Figure 6a), it is critical to understand when and where groundwater recharge occurs in order to ensure the persistence of the water and geothermal resources. The issue of groundwater recharge and resources has been extensively studied in the Atacama region (20°S) of northern of Chile (see Viguier et al. (2019) and references therein), which is analogous to the Tacna region. Due to the arid climate of the region since at least the middle Miocene (Houston & Hartley, 2003), past pluviometry in the region should be close to the current values, that is, 0–200 mm/yr for the coast and the forearc, and 200–650 mm/yr in the High Cordillera (Rau et al., 2017). Despite low precipitation levels, it has been demonstrated that the groundwater in neighboring systems in the Central Andes derived from rainwater and snow melt from the volcanic High Cordillera and the Precordillera (Bout et al., 2016; Magaritz et al., 1990), or even from the Coastal Cordillera (see Figure 1, Herrera et al. (2018)). If this limited recharge is sufficient to sustain the entire hydrothermal systems its longevity is ensured for thousands of years.

However, several authors suggest that past recharge of groundwater in North Chile could rather be related to extraordinary climate events such as glaciations or raining events. The Last Local Glacial Maximum (LLGM), which occurred 24 kyr ago, with additional incursions between 21–18 and 17–14 kyr ago (Ward et al., 2017), led to wetter conditions (Kull & Grosjean, 2000). During this period, the snow line elevation in the Tacna region was continuous above 4,600 m unlike the widespread current distribution on the highest peaks at 5,100 m (Klein et al., 1999). The subsequent deglaciation period could have resulted in massive water recharge into the faults, reaching depths of up to 10 km (Alt-Epping et al., 2021; Maréchal et al., 1999; Volpi et al., 2017). This last major deglaciation event could explain the apparent age of the Geisers springs (20.7 kyr), that is also suggested by Muñoz-Saez et al. (2020) about the nearby El Tatio geothermal field (Chile).

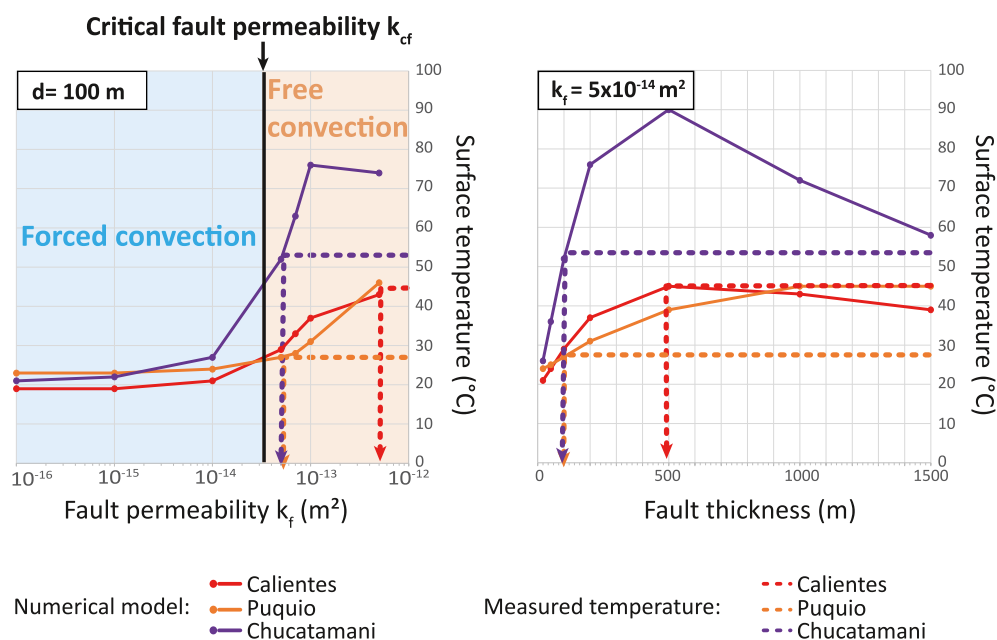


Figure 11. Temperatures measured on the model surface at the location of the Calientes, Puquiu, and Chucamatani springs as a function of, (a) the fault permeability (for a fault thickness $d = 100$ m, the critical fault permeability k_{cf} calculated in Section 4.2.1 separates the free and forced convection domains), (b) the fault thickness (for a fault permeability $k_f = 5 \times 10^{-14}$ m², slightly above the critical permeability). The colored arrows show parameter value allowing to reproduce the temperatures of the springs measured on the field (dot lines).

In addition, exceptional precipitation events known as the Central Andean Pluvial Event CAPE I (17.5–14.2 kyr BP) and CAPE II (13.8–9.7 kyr BP, Placzek et al. (2009); González-Pinilla et al. (2021)) may have constituted a substantial recharge. The latter event corresponds to the apparent ages of the Ticaco spring, and possibly to the Puquiu spring and IR146 well in la Yarada (Figure 6b), if they were rejuvenated by mixing with shallow groundwater.

The fluids of the Calientes springs, with a recharge elevation below 3,000 m and a recent age of 1.4 kyr (Figure 6), indicate that the geothermal loop is local and could not be influenced by ice melting other than the snow on the Chupiquiña and Tacora volcanoes. This is supported by the short distances covered by the flow lines in the numerical models, which are limited to a maximum of 3 km (Figures 9a and 10b). The Medieval Climate Anomaly in Atacama (1.01–0.71 kyr, Gayo et al. (2012)) could be the exceptional event that contributed to the Calientes springs, aligning with Herrera et al. (2018) in the Atacama.

If deglaciation or extreme precipitation events associated with the El Niño Southern Oscillation fluctuations contribute to the recharge of the Tacna hydrothermal systems, we can assume that it is subject to variability. The total budget is likely related to both mechanisms, with exceptional rainfall events affecting groundwater recharge on a timescale of 10–100 years (Boutt et al., 2016) and deep groundwater flows originating from the High and Cordillera over periods of 10–100 kyrs (Fritz et al., 1981; Jayne et al., 2016).

The hydrothermal model shows that the generation of orogenic hot springs from surface groundwater is highly dependent on the ability of the faults to ensure their recharge and circulation. The following section discusses the fault permeability and thickness through the results of the numerical model and a sensitivity analysis.

5.5. Fault Permeability and Damage Zone Thickness, and Fluid Flow Dynamic

A sensitivity study was conducted on the two primary parameters that are likely to affect thermal circulation, for which there is no field constraint: the fault permeability and the thickness of the fault damage zone (Figure 11).

In the cases of an unfaulted basement, or with impermeable faults, springs are not replicated on the model surface (Figure 8a). As suggested by the Ra number (Section 4.2.1), topography-driven flow in the basement is not sufficient to generate springs. However, when permeable faults are combined with elevated topographic gradients

along the fault planes (Section 4.2.1 and Figure 10), the model successfully replicates the location of the Chucamani, Calientes and Puquio springs (Figure 8b). The location of thermal anomalies remains constant regardless of permeability, indicating topography as the primary controlling factor. However, Figure 11a shows that the modeled temperature at the spring location increases with the permeability of the faults, starting to appear for values slightly below the critical fault permeability that marks the transition from forced to free convection ($k_{cf} \sim 3\text{--}4 \times 10^{-14} \text{ m}^2$, see Section 4.2.1). The comparison of spring temperatures in the field and in the model suggests that both forced and free convection are necessary to generate sufficiently elevated temperatures. In the cases of Puquio and Incaquiuo, the fault permeability is likely close to the critical level and the forced convection could be sufficient. However, it is likely that the Calientes springs require buoyancy to reach the observed temperatures.

The fault-valve behavior, which describes the subsequent co-seismic enhancement and inter-seismic reduction of the permeability (Im et al., 2018; Sibson, 1981), is inadequate to explain the continuous activity of hydrothermal springs during long inter-seismic periods. Evidence of thermal springs, fluids and associated deformation of isotherms in both fault compartments, indicate the occurrence of longitudinal and transverse hydrothermal circulations along reverse faults (Forster & Evans, 1991; Grasby & Hutcheon, 2001; Moretti et al., 2000; Rowe et al., 2009; Smeraglia et al., 2022). Accordingly, we propose that the Calientes and Incaquiuo faults may have a permanent and efficient permeability, transversely as well as longitudinally, even during inter-seismic periods. This supports the apparent fluid communication between the High Cordillera recharge with the Central Depression aquifers such as la Yarada (Figure 6b, see Section 5.2) and aligns with Prostka et al. (1982) and F. Aron et al. (2010) conclusions in the Central Cordillera. Additionally, N_2 is observed along the faults in this study (Figure 5) and in similar conditions in Peru and Bolivia as the dominant gas. It is suspected to be of atmospheric origin and to be infiltrated along faults (Hiatt et al., 2022; Labidi et al., 2021). This constitutes a supplementary evidence of particularly efficient permeability in the recharge zones. Other hypotheses propose release of N_2 through sediment incorporation along the slab (Munoz-Saez et al., 2020), supporting the idea of a crustal extension of the permeability of the faults.

The thickness of the fault damage zone also greatly influences the temperature at the model surface (Figure 11b). For a range of expected values for regional faults (Savage & Brodsky, 2011), the surface temperature increases up to a maximum of 500–1,000 m in this simulation. Afterward, the temperature decreases due to the infiltration of cold superficial fluids along the fault planes. The expected damage zone thickness for the Calientes and Incaquiuo faults is a maximum of 1,000 m. For larger damage zones than shown in Figure 8b, the thermal anomalies are also larger.

The permeability and the thickness of the damage zone of the faults are likely not uniform throughout the entire fault network, or even along the same fault. The sensitivity analysis revealed that the Calientes fault at Calientes may be more permeable and/or have a more developed fault zone than in Puquio (Figure 11). This difference could be explained by the Calientes fault's tectonic propagation over time from SE to NW (Figure 1a and Hall et al. (2012)), which results in a better development of the damage zone near the center (near Calientes) than at the tips (W of Puquio, see Torabi and Berg (2011)). The sequences and locations of fault reactivation may have caused varying levels of damage along the faults or re-opening of sealed zones. At a smaller scale, local complexities (e.g., faults and fracture connectivity, fracture sealing, fault zone size) explain the difference between the large extension of the thermal anomalies at the model surface (Figure 8b) compared to the concentration of the observed springs. All of these hypotheses should be validated by geological and structural observations of the fault zones, as well as a deeper understanding of recent and current activity on the Calientes and Incaquiuo faults, integrated into a more complex numerical model.

5.6. Limits of the Numerical Model and Future Developments

In this first version of the numerical model, several simplifications were made, as explained in Section 3.2. As is typical in hydrothermal simulations (e.g., Guillou-Frotier et al. (2013); Magri et al. (2016)), the model depth was adjusted to maintain pressure and temperature conditions where the fluid remain in a liquid state. Furthermore, the model did not account for the high temperatures caused by the presence of magma below volcanoes, which resulted in the inability to replicate the Aruma, Geiser, and Barroso springs. Accordingly, equations of state are adapted to liquid conditions and neglect the effects of pressure and salinity. Future models will be built with a

deeper geometry, limiting boundary effects, and will integrate multi-phase conditions and adapted equations of state, such as those used in Launay et al. (2023).

In order to upgrade the model, better geological constraints are necessary. Faults have been oversimplified as straight planes with homogeneous dip, fault zone thickness, and permeability, which is not accurate. Forearc faults often show a steep dip at the surface and acquire a listric form at depth before rooting with other faults. Fault permeability varies not only along the fault as discussed in Section 5.5, but also with depth due to the closure of the fractures under the effect of the confining pressure, and even within the fault zone (Caine et al., 1996). Furthermore, this simulation only considered three main faults, while the regional fault network appears to be more complex (Figure 1a). This statement is important because fault interaction or intersection could promote hydrothermal circulations (Curewitz & Karson, 1997). Finally, this simulation considered that the host-rock permeability is homogeneous. However, fault-related springs are typically found within the fractured Cretaceous crystalline rocks near the contact with volcano-clastic rocks (Figures 1a, 1d, 2c, and 2d). Crystalline rocks are often identified as favoring fluid circulations in orogenic belt hydrothermal systems (e.g., in the Atacama (Scheiing et al., 2017; Urrutia et al., 2019) or in the European Alps (Taillefer et al., 2021; Wanner et al., 2020)). Some of the thermal anomalies that are observed on the model surface, but not in the field (e.g., the Laguna Aricota lake, Figure 8b), could be related to the impermeable cap formed by volcano-clastic rocks (Figures 1a and 1d). Although faults may exist in the volcanic chain, allowing meteoric and magmatic fluids to circulate between the surface and the magma chambers, they are not mapped or obscured by recent volcanic rocks (Figures 1a and 1d).

Future models will incorporate a detailed geological model featuring a complex fault network with accurate properties (e.g., Taillefer et al., 2018), lateral variations of lithologies (e.g., Magri et al., 2016), and the presence of magma chambers (e.g., Byrdina et al., 2013). Others aspects, such as the impact of the regional stress (e.g., Duwiquet et al., 2021) or transient effects related to seismic activity (e.g., Lupi et al., 2011), could also be explored. Nevertheless, this preliminary model accurately replicates the locations and temperatures of most springs located on the modeled faults and enables analysis of the primary processes at work. This allows to propose the first conceptual model of the Tacna hydrothermal systems and to discuss its implications for the regional geothermal potential.

5.7. Conceptual Model of the Tacna Hydrothermal Systems

By comparing our findings with the results of the numerical modeling, we propose a conceptual model of the hydrothermal systems in the Tacna region (Figure 12). Fluid recharge zones, mostly glacial or rain-fed, are located between 2000 and 4,500 m altitude. Volcanic hydrothermal systems exhibit a distinct geochemical signature, characterized by the predominant release of CO₂ and the partial contribution of magmatic fluids, indicating the proximity and influence of magma at depth. The hydrothermal loop is likely to be short and local. Infiltration of meteoric fluids occurs on volcanoes near thermal springs. The proximity of volcanic magma acts as a heat source that is anomalously higher than the ambient geothermal gradient, inducing high spring temperatures and high TDS, but confined to the High Cordillera.

In contrast, the thermal springs located in the forearc orogenic belt exhibit more diverse geochemical signatures. The fluids that supply these systems are strictly meteoric and circulate along permeable faults where they intersect recharge zones or are captured from aquifers in the surrounding rocks. It is possible that the N₂ predominantly observed in forearc springs, likely atmospheric, is dissolved in the water at this stage. The consequent topographic gradient is primary factor that controls fluid circulation along faults and in surrounding rocks. Regional faults create large hydrothermal loops, where fluids are heated up by the local geothermal gradient, resulting in the thermal springs observed in the field. The variety of geochemical signatures observed can be explained by the different paths taken by these fluids. The geochemical signature similarities observed between the Ticaco and Chucutamani springs and the Yarada wells near the shoreline suggest the possibility of transverse circulation across faults, indicating their significant permeability.

Finally, the geothermal gradient is not sufficient to heat the Aruma fluids, so the magma chamber must also contribute the heat budget. These fluids are driven along the Incapuquio fault by the topographic gradient and potentially the North-dipping Mesozoic series (Figure 1d). They could then flow toward the Precordillera (Figures 9, 10, and 12).

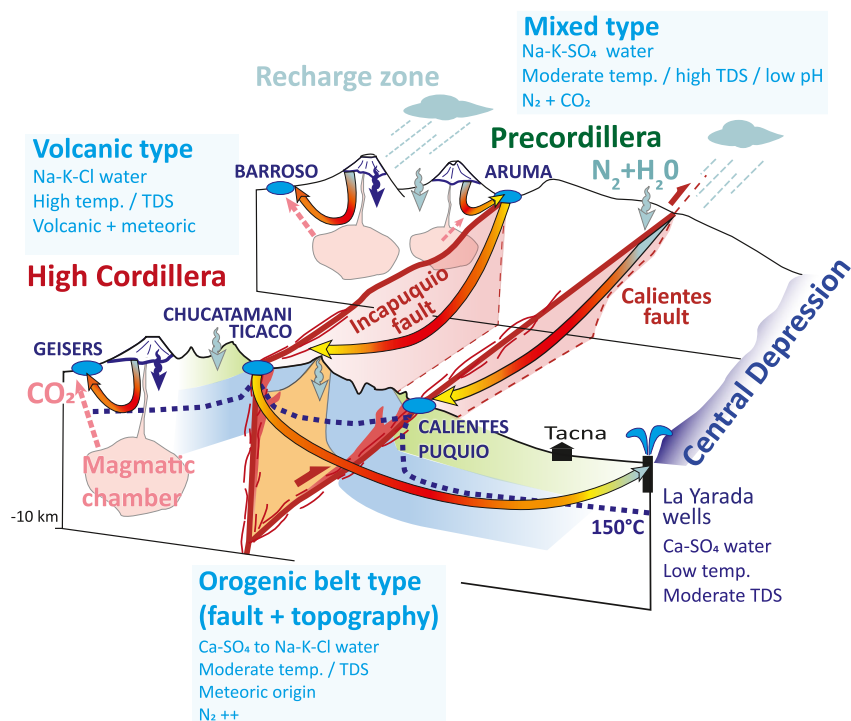


Figure 12. Conceptual model of the Tacna hydrothermal systems. Thermal springs (blue circles) are associated with two distinct hydrothermal systems. The volcanic type has volcanic geochemical signature and is located in the High Cordillera. The short hydrothermal loops (colored arrows) of this system require heat from the magma chambers, where the CO_2 (pink arrows) originates. The orogenic belt type has varied geochemical signatures but is solely of meteoric origin. It is located in the forearc and its long loops develop along and transversely to permeable active faults, in response to strong topographic gradients. Glacial and precipitation recharge zones (dark and light blue arrows, respectively) are located at high elevations and captured along fault planes, possibly at the same time as N_2 . Mixed systems may combine features of the two previous types. These systems induce significant deformations of the isotherms in the region (blue dashed line).

The effects of these complex interactions between magmatism, faulting, and topography on hydrothermal system differentiation have also been evidenced in other Peruvian provinces, such as the Arequipa region (Alvarez-Campos et al., 2022; Tyc et al., 2022) and the Cordillera Blanca (Scott et al., 2020). These hydrothermal circulations induce significant deformations of the isotherms. The geothermal gradient increases near volcanoes, as well as along faults where thermal springs are located. On the other hand, it decreases in infiltration zones along faults when the topographic gradient is significant.

5.8. The Geothermal Potential of the Andean Forearc in the Tacna Region

Electricity or direct-use geothermal projects preferentially target on accessing abnormally hot aquifers that are close to the surface and to the end-users, in order to minimize drilling and operational costs. Additionally, it is advisable to drill outside of seismogenic faults to limit the risk of induced seismicity by fluid injection. The best location meeting these criteria to supply the Tacna city would be an aquifer connecting the hydrothermal flow along the Calientes fault with the Central Depression, which would explain the abnormally high temperatures of the la Yarada wells.

To obtain a clear idea of the lateral extent and depth of the thermal anomalies generated by the faults, we have extracted out of our numerical model with $k_f = 5 \times 10^{-14} \text{ m}^2$, the elevation of the 150°C isotherm (i.e., the temperature for geothermal electricity generation, Figure 13).

On a regional scale, outside the fault zones and spanning hundreds of kilometers, the elevation of the 150°C isotherm approximately follows the topography (i.e., the imposed geothermal gradient, here 50°C/km). Precise elevations and depths below the surface of the 150°C (geothermal electric generation) and 80°C (geothermal direct heat use) isotherms in strategic locations are available in Table S6 in Supporting Information S2. The hot

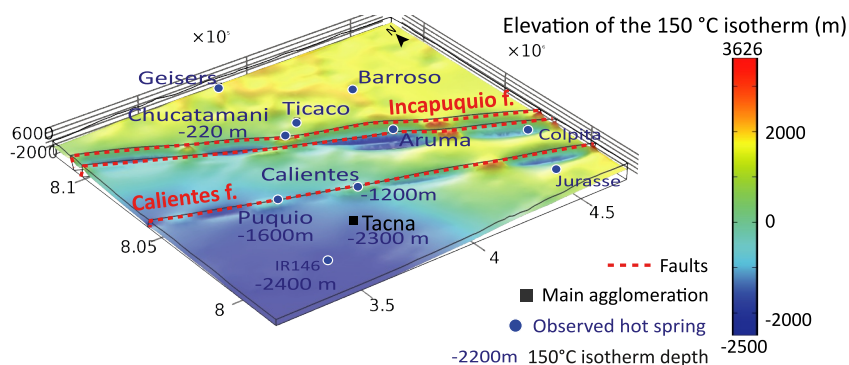


Figure 13. Elevation of the 150°C iso-surface. Blue and red zones correspond to a collapse or an upwelling of the 150°C isotherm, respectively. Blue numbers indicate the depth of the 150°C isotherm below the strategic points (see Table S6 in Supporting Information S2).

plumes observed in Figure 10 zones cause a rise of the 150°C isotherm along the faults. The extent of perturbation radius can span tens of kilometers, depending on the plume wavelengths and of the fault zone thickness. The 150°C isotherm is very close to the surface beneath the springs (e.g., ~1,000 m deep at Calientes), highlighting the high geothermal potential of fault forearc as suggested in the Eastern Precordillera in Argentina (30–280 kW, Christiansen et al. (2021)).

Beyond the influence of the faults, the impact of the Calientes or Puquio plumes on the temperatures at depth below the Tacna city seems limited: the 150°C isotherm reaches the depths of 2,300 m, which remains an acceptable depth for geothermal drilling in basins (e.g., the Parisian basin).

The interpretation of depth, temperatures and the lateral extent of the thermal anomaly distribution in the Tacna region must be nuanced due to our limited knowledge about the size of the fault zones, the local geothermal gradient and basal heat flow, and about the complexity of the aquifers in the Central Depression. The high potential associated with faults could exert a more substantial influence if we assume a connection between the fluids circulating along these faults and the aquifers tapped by the la Yarada wells as suggested by flow lines in the numerical model (Figure 9). This highlights the need for further investigations of the hydrogeological context in this zone, which is also critical for the management of the shallow water resource.

6. Conclusion

This study aims to constrain geothermal potential of inhabited areas of the Tacna (South of Peru) region by deciphering the contributions of volcanoes, faults, and topography on the hydrothermal systems.

On one hand, the geochemical data indicates that:

- The springs located near active volcanoes in the High Cordillera are characterized by Na-K-Cl water with high temperatures of both emergence (up to 87°C) and reservoir (mean of 170°C), and high TDS (up to 3,452 mg/L). The free gas phase is mainly composed of CO₂ (>90 vol%). Isotopic data indicates mixed meteoric and volcanic origins, and radiocarbon suggests an approximate age of 20.7 kyr.
- Springs located in the forearc in the Precordillera are aligned along regional faults. They show Ca-SO₄ and Na-K-Cl compositions with moderate temperatures of both emergence (27–53°C) and reservoir (mean of ~100°C), and intermediate TDS values (up to 2,458 mg/L). The gas composition is largely dominated by N₂ (>95 vol%). Isotopic data indicate a purely meteoric origin and radiocarbon ages are between 1.4 and 7.9 kyr. Irrigation wells in the forearc basin display similar features, despite low emergence temperature (30–32°C) for higher reservoir temperature (~140°C)
- The Aruma spring located in the volcanic High Cordillera along the Incapuquio fault shows intermediate features between the volcanic and forearc springs: Na-K-SO₄ water with elevated temperatures of both emergence (45–64°C) and reservoir (mean of 167°C), high TDS (3,642–3,397 mg/L) and pH of 2. The gas phase shows a mixed composition comprising 20–40 vol% of CO₂ and 60–80 vol% of N₂.

On the other hand, the regional 3D numerical model highlights that both forced and free convections occur along and throughout faults with high permeability ($>10^{-14} \text{ m}^2$). This results in the formation of 100-km long thermal plumes replicating the observed springs in the forearc, and upwelling of the 150°C isotherm (i.e., the temperature for geothermal electricity generation) to within $\sim 1,000 \text{ m}$ of the surface.

The models provide valuable insights into the origin and pathways of the hydrothermal fluids shedding light on the geochemical similarities of the different springs. This allows us to propose and discuss a conceptual model of the Tacna region hydrothermal systems where the volcanic springs are sustained by the heat of magma chambers although the geothermal gradient and topography or buoyancy-driven convections are sufficient to generate thermal anomalies within permeable faults. To improve the evaluation of geothermal potential and accurately replicate all sources in the Tacna region, future models must incorporate a more complex fault network with decreasing permeabilities in faults, lateral variation of lithologies, and magma chambers, requiring thicker models and EOS adapted to multiphase fluids. This study also demonstrates the potential of reverse faults to generate substantial geothermal anomalies in compressive contexts, opening perspectives for the geothermal exploration throughout the entire forearc of the Andean Cordillera.

Appendix A: Governing Equations in Numerical Models

The COMSOL Multiphysics™5.2 software numerically couples the Darcy law and the heat transfer equation, treating the model as a permeable and porous medium.

The heat transfer equation for homogeneous and isotropic medium, considering convective transfers, is:

$$\rho_m C_p \frac{\partial T}{\partial t} = \lambda \Delta T + A - \rho_f C_{l_f} \vec{\nabla} T \cdot \vec{v} \quad (\text{A1})$$

with T (°C) the temperature, ρ_m (kg/m^3) the media mass density, C_p ($\text{J}/(\text{kg}\cdot\text{K})$) the media specific heat capacity, λ the media thermal conductivity ($\text{W}/(\text{m}\cdot\text{K})$) and A (W/m^3) the heat production, $\vec{\nabla} T \cdot \vec{v}$ an advective term, ρ_f (kg/m^3) the fluid mass density and C_{l_f} ($\text{J}/(\text{kg}\cdot\text{K})$) the fluid specific heat.

For porous and permeable media the Darcy law describes fluids motion driven by a pressure gradient such as:

$$\vec{u} = \frac{k}{\mu} (\vec{\nabla} p - \rho_f \vec{g}) \quad (\text{A2})$$

with \vec{u} the fluid velocity, k (m^2) the medium permeability, ν (m^2/s) the fluid cinematic viscosity, $\vec{\nabla} p$ the pressure gradient, ρ_f (kg/m^3) the fluid mass density, and \vec{g} the acceleration of gravity.

Fluid is supposed incompressible and so mass conservation writes $\vec{\nabla} \cdot \vec{u} = 0$, equivalent to:

$$\vec{\nabla} \cdot \left[-\frac{k}{\mu} (\vec{\nabla} p + \rho_f \vec{g}) \right] = 0 \quad (\text{A3})$$

The coupling between heat transfer equation and Darcy law occurs through the fluid velocity field, that is, $\vec{\nabla} T \cdot \vec{v}$ in Equation A1, and \vec{u} in Equations A2 and A3. Further, temperature (the other coupling variable) appears in Equations A1 and A2, since ρ_f and μ are temperature-dependent.

Appendix B: Critical Rayleigh Number and Critical Permeability

For an infinitely long homogeneous porous medium (Lapwood, 1948), Ra is defined as:

$$Ra = \frac{K L \alpha \Delta T}{D_\lambda} \quad (\text{B1})$$

where K (m/s) is the hydraulic conductivity, related to the permeability k (m^2) by:

$$k = K \frac{\mu}{\rho_f g} \quad (\text{B2})$$

L (m) is the thickness of the medium in which the flow takes place, $\alpha = 10^{-4} \text{ K}^{-1}$ the coefficient of thermal expansion and ΔT ($^{\circ}\text{C}$) the difference in temperature between the upper and lower limits of the medium. The tensor of thermodispersion D_λ is defined by:

$$D_\lambda = \frac{\Phi \lambda_f + (1 - \Phi) \lambda_s}{\rho_f C p_f} \quad (\text{B3})$$

where Φ is the porosity, ρ_f (kg/m^3) the fluid density, $C p_f$ ($\text{J}/(\text{kg}\cdot\text{K})$) the thermal capacity of the fluid, and λ_f and λ_s ($\text{W}/(\text{m}\cdot\text{K})$) the fluid and solid thermal conductivity, respectively.

Additionally, for a finite medium including faults, the critical Rayleigh number depends on the faults' dimensions and can be expressed by the ratio between the fault width and height. An analytical expression to calculate Ra_c of 3D faults has been proposed by Malkovsky and Pek (2004):

$$Ra_{cf} = \left[\left(\frac{6.428}{\Delta} \right)^{1.165} + (27.1)^{1.165} \right]^{0.8584}, \text{ with } \Delta = \frac{d}{2H} < 0.1 \quad (\text{B4})$$

Δ is half the fault aspect ratio, with d (m) the width of the fault zone and H (m) the fault high between its elevation on the surface and the model base.

Finally, analytical and numerical simulations by Malkovsky and Magri (2016) show that the critical fault permeability k_{cf} at which convection is likely to start within faults is calculated by assuming $Ra_{cf}/4$ (e.g., their Figure 4) in compilations of Equation B1, B3, and B4.

Data Availability Statement

The whole geochemical data and numerical results are given in Supporting Information S1: Table S1 in Supporting Information S2: ionic composition of the thermal water; Table S2 in Supporting Information S2: details of free gases composition; Table S3 in Supporting Information S2: details of dissolved gases composition; Table S4 in Supporting Information S2: isotopic composition of the thermal water; Table S5 in Supporting Information S2: calculation details of geothermometers; Table S6 in Supporting Information S2: depths of the 150°C and 80°C isotherms in the numerical models at strategic points. Figure S1 in Supporting Information S1: values of pressure and temperature in a computed model. The geochemical data set is available in the EarthChem Library (Taillefer et al., 2024).

Acknowledgments

This work was funded by IRD (the French National Research Institute for Sustainable Development) and by the ISTerre Laboratory of the Grenoble Alpes University (UGA), which we thank for their financial and technical support. L. Truche acknowledges support from the Institut Universitaire de France. The authors also thank INGEMMET for their help on the field. We thank S. Byrdina, K. Gaidzik, F. Magri and L. Guillou-Frottier, who help to greatly improve the manuscript.

References

- Acosta, H., Alván, A., Mamani, M., Oviedo, M., & Rodriguez, J. (2011). Geología de los cuadrángulos de Pachía y Palca. *Boletín N 139 Serie A-Ingemmet*, 83.
- Allmendinger, R. W., González, G., Yu, J., Hoke, G., & Isacks, B. (2005). Trench-parallel shortening in the northern Chilean forearc: Tectonic and climatic implications. *Geological Society of America Bulletin*, 117(1–2), 89–104. <https://doi.org/10.1130/B25505.1>
- Alt-Epping, P., Diamond, L. W., Wanner, C., & Hammond, G. E. (2021). Effect of glacial/interglacial recharge conditions on flow of meteoric water through deep orogenic faults: Insights into the geothermal system at Grimsel Pass, Switzerland. *Journal of Geophysical Research: Solid Earth*, 126(7), e2020JB021271. <https://doi.org/10.1029/2020JB021271>
- Alván, A., Jacay, J., Caracciolo, L., Sánchez, E., & Trinidad, I. (2018). Sedimentary facies analysis of the Mesozoic clastic rocks in Southern Peru (Tacna, 18°S): Towards a paleoenvironmental redefinition and stratigraphic reorganization. *Journal of South American Earth Sciences*, 84, 399–421. <https://doi.org/10.1016/j.jsames.2018.04.014>
- Alvarez-Campos, O., Olson, E. J., Welp, L. R., Frisbee, M. D., Zuñiga Medina, S. A., Díaz Rodríguez, J., et al. (2022). Evidence for high-elevation salar recharge and interbasin groundwater flow in the Western Cordillera of the Peruvian Andes. *Hydrology and Earth System Sciences*, 26(2), 483–503. <https://doi.org/10.5194/hess-26-483-2022>
- Ambach, W., Dansgaard, W., Eisner, H., & Møller, J. (1968). The altitude effect on the isotopic composition of precipitation and glacier ice in the Alps. *Tellus*, 20(4), 595–600. <https://doi.org/10.3402/tellusa.v20i4.10040>
- Arnórsson, S., Gunnlaugsson, E., & Svavarsson, H. (1983). The chemistry of geothermal waters in Iceland. II. Mineral equilibria and independent variables controlling water compositions. *Geochimica et Cosmochimica Acta*, 47(3), 547–566. [https://doi.org/10.1016/0016-7037\(83\)90277-6](https://doi.org/10.1016/0016-7037(83)90277-6)
- Aron, F., González, G., Cembrano, J., & Veloso, E. (2010). Reverse faulting as a crucial mechanism for magma ascent in compressional volcanic arcs: Field examples from the Central Andes. In *AGU fall meeting abstracts, 2010* (p. V43B-2379).

- Aron, P. G., Poulsen, C. J., Fiorella, R. P., Levin, N. E., Acosta, R. P., Yanites, B. J., & Cassel, E. J. (2021). Variability and controls on $\delta^{18}\text{O}$, d -excess, and $\delta^{17}\text{O}$ in southern Peruvian precipitation. *Journal of Geophysical Research: Atmospheres*, 126(23), e2020JD034009. <https://doi.org/10.1029/2020JD034009>
- Audin, L., David, C., Hall, S., Farber, D., & Hérail, G. (2006). Geomorphic evidences of recent tectonic activity in the forearc, southern Peru. *Revista de la Asociación Geológica Argentina*, 61(4), 545–554.
- Audin, L., Lacan, P., Tavera, H., & Bondoux, F. (2008). Upper plate deformation and seismic barrier in front of Nazca subduction zone: The Cholo Fault System and active tectonics along the Coastal Cordillera, Southern Peru. *Tectonophysics*, 459(1–4), 174–185. <https://doi.org/10.1016/j.tecto.2007.11.070>
- Audin, L., Perfettini, H., Avouac, J., Farber, D., De la Cruz, D., & Chlieh, M. (2007). The 2007 Pisco earthquake (Mw8.0), Central Peru: Preliminary field investigations and seismotectonic context. In *Eos transactions AGU, fall meeting Supplement* (Vol. 88, p. T33E-02).
- Belgrano, T. M., Herwegh, M., & Berger, A. (2016). Inherited structural controls on fault geometry, architecture and hydrothermal activity: An example from Grimsel Pass, Switzerland. *Swiss Journal of Geosciences*, 109(3), 345–364. <https://doi.org/10.1007/s00015-016-0212-9>
- Bellido, E. (1969). Sinopsis de la geología del Perú. *INGEMMET. Boletín, Serie A: Carta Geológica Nacional*, 22.
- Benavente, C., Palomino, A., Wimpenny, S., García, B., Rosell, L., Aguirre, E., et al. (2022). Paleoseismic evidence of the 1715 CE earthquake on the Purgatorio Fault in Southern Peru: Implications for seismic hazard in subduction zones. *Tectonophysics*, 834, 229355. <https://doi.org/10.1016/j.tecto.2022.229355>
- Benavente, C., Wimpenny, S., Rosell, L., Robert, X., Palomino, A., Audin, L., et al. (2021). Paleoseismic evidence of an Mw 7 pre-Hispanic earthquake in the Peruvian forearc. *Tectonics*, 40(6), e2020TC006479. <https://doi.org/10.1029/2020TC006479>
- Benavente, C., Zerathe, S., Audin, L., Hall, S. R., Robert, X., Delgado, F., et al. (2017). Active transpressional tectonics in the Andean forearc of southern Peru quantified by ^{10}Be surface exposure dating of an active fault scarp. *Tectonics*, 36(9), 1662–1678. <https://doi.org/10.1002/2017TC004523>
- Boekhout, F., Sempéré, T., Spikings, R., & Schaltegger, U. (2013). Late Paleozoic to Jurassic chronostratigraphy of coastal southern Peru: Temporal evolution of sedimentation along an active margin. *Journal of South American Earth Sciences*, 47, 179–200. <https://doi.org/10.1016/j.jsames.2013.07.003>
- Boschetti, T., Cifuentes, J., Iacumin, P., & Selmo, E. (2019). Local meteoric water line of Northern Chile (18 S–30 S): An application of error-invariables regression to the oxygen and hydrogen stable isotope ratio of precipitation. *Water*, 11(4), 791. <https://doi.org/10.3390/w11040791>
- Boutt, D. F., Hynke, S. A., Munk, L. A., & Coresenthal, L. G. (2016). Rapid recharge of fresh water to the halite-hosted brine aquifer of Salar de Atacama, Chile. *Hydrological Processes*, 30(25), 4720–4740. <https://doi.org/10.1002/hyp.10994>
- Byrdina, S., Ramos, D., Vandemeulebrouck, J., Masias, P., Revil, A., Finizola, A., et al. (2013). Influence of the regional topography on the remote emplacement of hydrothermal systems with examples of Ticsani and Ubina volcanoes, Southern Peru. *Earth and Planetary Science Letters*, 365, 152–164. <https://doi.org/10.1016/j.epsl.2013.01.018>
- Caine, J. S., Evans, J. P., & Forster, C. B. (1996). Fault zone architecture and permeability structure. *Geology*, 24(11), 1025–1028. [https://doi.org/10.1130/0091-7613\(1996\)024\(1025:FZAAPS\)2.3.CO;2](https://doi.org/10.1130/0091-7613(1996)024(1025:FZAAPS)2.3.CO;2)
- Chavez, C., Roddaz, M., Dantas, E. L., Santos, R. V., & Alván, A. A. (2022). Provenance of the middle Jurassic-Cretaceous sedimentary rocks of the Arequipa basin (South Peru) and implications for the geodynamic evolution of the central Andes. *Gondwana Research*, 101, 59–76. <https://doi.org/10.1016/j.gr.2021.07.018>
- Chen, Y.-W., Wu, J., & Suppe, J. (2019). Southward propagation of Nazca subduction along the Andes. *Nature*, 565(7740), 441–447. <https://doi.org/10.1038/s41586-018-0860-1>
- Christiansen, R. O., Clavel, F., Gonzalez, M., García, H. P., Ortiz, D. A., Ariza, J. P., et al. (2021). Low-enthalpy geothermal energy resources in the central Andes of Argentina: A case study of the Pismanta system. *Renewable Energy*, 177, 1234–1252. <https://doi.org/10.1016/j.renene.2021.06.065>
- Chucuya, S., Vera, A., Pino-Vargas, E., Steenken, A., Mahlknecht, J., & Montalván, I. (2022). Hydrogeochemical characterization and identification of factors influencing groundwater quality in coastal aquifers, case: La Yarada, Tacna, Peru. *International Journal of Environmental Research and Public Health*, 19(5), 2815. <https://doi.org/10.3390/ijerph19052815>
- Cioni, R., & Marini, L. (2020). Traditional water geothermometers and CO_2 - indicators. In *A thermodynamic approach to water geothermometry* (pp. 225–332). Springer. https://doi.org/10.1007/978-3-030-54318-1_5
- Cobbing, E. J., Ozard, J., & Snelling, N. (1977). Reconnaissance geochronology of the crystalline basement rocks of the Coastal Cordillera of Southern Peru. *Geological Society of America Bulletin*, 88(2), 241–246. [https://doi.org/10.1130/0016-7606\(1977\)88\(241:RGOTCB\)2.0.CO;2](https://doi.org/10.1130/0016-7606(1977)88(241:RGOTCB)2.0.CO;2)
- Cobbing, E. J., & Pitcher, W. S. (1972). The coastal Batholith of Central Peru. *Journal of the Geological Society*, 128(5), 421–454. <https://doi.org/10.1144/gsjgs.128.5.0421>
- Cortecci, G., Boschetti, T., Mussi, M., Lameli, C. H., Mucchino, C., & Barbieri, M. (2005). New chemical and original isotopic data on waters from El Tatio geothermal field, Northern Chile. *Geochemical Journal*, 39(6), 547–571. <https://doi.org/10.2343/geochemj.39.547>
- Craig, H. (1961). Isotopic variations in meteoric waters. *Science*, 133(3465), 1702–1703. <https://doi.org/10.1126/science.133.3465.1702>
- Cruz, V. (2018). Chemical and isotopic composition of hot spring waters in the Tacna region, Southern Peru. *INGEMMET, Technical Report*.
- Cruz, V., & Ollascoaga, D. (2021). Caracterización geoquímica de los manantiales geotermiales de la zona de Paucarani, Región Tacna, Perú. In *Publicación Especial N° 15—Resúmenes ampliados del XX Congreso Peruano de Geología*.
- Cruz, V., & Vargas, V. (2015). Geothermal Country update for Peru, 2010–2014. In *Proceedings world geothermal congress 2015*.
- Cruz, V., Vargas, V., & Matsuda, K. (2010). Geochemical characterization of thermal waters in the Calientes geothermal field, Tacna, South of Peru. In *Proceedings world geothermal congress 2010, Bali, Indonesia*.
- Curewitz, D., & Karson, J. A. (1997). Structural settings of hydrothermal outflow: Fracture permeability maintained by fault propagation and interaction. *Journal of Volcanology and Geothermal Research*, 79(3–4), 149–168. [https://doi.org/10.1016/s0377-0273\(97\)00027-9](https://doi.org/10.1016/s0377-0273(97)00027-9)
- David, C., Audin, L., Comte, D., Tavera, H., & Hérail, G. (2005). Crustal seismicity and active tectonics in the Arica bend forearc. In *6th international symposium on Andean geodynamics (ISAG 2005, barcelona)* (Vol. 206, p. 210). extended abstracts.
- Delgado, F., Zerathe, S., Audin, L., Schwartz, S., Benavente, C., Carcaillet, J., et al. (2020). Giant landslide triggerings and paleoprecipitations in the central western Andes: The Aricota rockslide dam (South Peru). *Geomorphology*, 350, 106932. <https://doi.org/10.1016/j.geomorph.2019.106932>
- Delgado, F., Zerathe, S., Schwartz, S., Mathieux, B., & Benavente, C. (2022). Inventory of large landslides along the Central Western Andes (ca. 15–20 s): Landslide distribution patterns and insights on controlling factors. *Journal of South American Earth Sciences*, 116, 103824. <https://doi.org/10.1016/j.jsames.2022.103824>
- Dickson, A. G. (1981). An exact definition of total alkalinity and a procedure for the estimation of alkalinity and total inorganic carbon from titration data. *Deep-Sea Research, Part A: Oceanographic Research Papers*, 28(6), 609–623. [https://doi.org/10.1016/0198-0149\(81\)90121-7](https://doi.org/10.1016/0198-0149(81)90121-7)

- Duwiquet, H., Guillou-Frottier, L., Arbaret, L., Bellanger, M., Guillon, T., & Heap, M. J. (2021). Crustal fault zones (CFZ) as geothermal power systems: A preliminary 3D THM model constrained by a multidisciplinary approach. *Geofluids*, 2021, 1–24. <https://doi.org/10.1155/2021/8855632>
- Evans, J. P., Forster, C. B., & Goddard, J. V. (1997). Permeability of fault-related rocks, and implications for hydraulic structure of fault zones. *Journal of Structural Geology*, 19(11), 1393–1404. [https://doi.org/10.1016/S0191-8141\(97\)00057-6](https://doi.org/10.1016/S0191-8141(97)00057-6)
- Evenstar, L., Mather, A. E., & Hartley, A. (2020). Using spatial patterns of fluvial incision to constrain continental-scale uplift in the Andes. *Global and Planetary Change*, 186, 103119. <https://doi.org/10.1016/j.gloplacha.2020.103119>
- Fischer, T. P., & Chiodini, G. (2015). Volcanic, magmatic and hydrothermal gases. In *The encyclopedia of volcanoes* (pp. 779–797). Elsevier. <https://doi.org/10.1016/B978-0-12-385938-9.00045-6>
- Forster, C. B., & Evans, J. P. (1991). Hydrogeology of thrust faults and crystalline thrust sheets: Results of combined field and modeling studies. *Geophysical Research Letters*, 18(5), 979–982. <https://doi.org/10.1029/91GL00950>
- Forster, C. B., & Smith, L. (1989). The influence of groundwater flow on thermal regimes in mountainous terrain: A model study. *Journal of Geophysical Research*, 94(B7), 9439–9451. <https://doi.org/10.1029/JB094iB07p09439>
- Fournier, R., & Potter, I. (1982). Revised and expanded silica (quartz) geothermometer. *Bulletin Geothermal Resources Council (Davis, Calif.); (United States)*, 11(10).
- Fournier, R. O. (1973). Silica in thermal waters: Laboratory and field investigations. In *International symposium on hydrogeochemistry and biochemistry proceedings, Tokyo* (Vol. 1, pp. 122–139).
- Fritz, P., Suzuki, O., Silva, C., & Salati, E. (1981). Isotope hydrology of groundwaters in the Pampa del Tamarugal, Chile. *Journal of Hydrology*, 53(1–2), 161–184. [https://doi.org/10.1016/0022-1694\(81\)90043-3](https://doi.org/10.1016/0022-1694(81)90043-3)
- Gaidzik, K., & Wiesek, M. (2021). Seismo-lineaments and potentially seismogenic faults in the overriding plate of the Nazca-South American subduction zone (S Peru). *Journal of South American Earth Sciences*, 109, 103303. <https://doi.org/10.1016/j.jsames.2021.103303>
- García, M., Aguilar, G., Rodríguez, M. P., & Metcalf, J. (2022). (U-Th)/He ages of proterozoic-paleozoic basement rocks from Northern Chile (18–19°S) and implications on the Neogene uplift history of the Western Cordillera. *Andean Geology*, 49(3), 313–326. <https://doi.org/10.5027/andgeoV49n3-3402>
- Gayo, E. M., Latorre, C., Jordan, T. E., Nester, P. L., Estay, S. A., Ojeda, K. F., & Santoro, C. M. (2012). Late Quaternary hydrological and ecological changes in the hyperarid core of the northern Atacama Desert (~21S). *Earth-Science Reviews*, 113(3–4), 120–140. <https://doi.org/10.1016/j.earscirev.2012.04.003>
- GEOCATMIN. (2022). INGEMMET. Retrieved from <https://geocatmin.ingemmet.gob.pe/geocatmin/>
- Giggenbach, W. (1988). Geothermal solute equilibria derivation of Na-K-Mg-Ca geoindicators. *Geochimica et Cosmochimica Acta*, 52(12), 2749–2765. [https://doi.org/10.1016/0016-7037\(88\)90143-3](https://doi.org/10.1016/0016-7037(88)90143-3)
- Gleeson, T., & Manning, A. H. (2008). Regional groundwater flow in mountainous terrain: Three-dimensional simulations of topographic and hydrogeologic controls. *Water Resources Research*, 44(10). <https://doi.org/10.1029/2008wr006848>
- González-Pinilla, F. J., Latorre, C., Rojas, M., Houston, J., Rocuant, M. I., Maldonado, A., et al. (2021). High-and low-latitude forcings drive Atacama Desert rainfall variations over the past 16,000 years. *Science Advances*, 7(38), eabg1333. <https://doi.org/10.1126/sciadv.abg1333>
- Grasby, S. E., & Hutcheon, I. (2001). Controls on the distribution of thermal springs in the southern Canadian Cordillera. *Canadian Journal of Earth Sciences*, 38(3), 427–440. <https://doi.org/10.1139/e00-091>
- Guillou-Frottier, L., Carré, C., Bourguin, B., Bouchot, V., & Genter, A. (2013). Structure of hydrothermal convection in the Upper Rhine Graben as inferred from corrected temperature data and basin-scale numerical models. *Journal of Volcanology and Geothermal Research*, 256, 29–49. <https://doi.org/10.1016/j.jvolgeores.2013.02.008>
- Guillou-Frottier, L., Duwiquet, H., Launay, G., Taillefer, A., Roche, V., & Link, G. (2020). On the morphology and amplitude of 2D and 3D thermal anomalies induced by buoyancy-driven flow within and around fault zones. *Solid Earth*, 11(4), 1571–1595. <https://doi.org/10.5194/se-11-1571-2020>
- Guillou-Frottier, L., Milesi, G., Roche, V., Duwiquet, H., & Taillefer, A. (2024). Heat flow, thermal anomalies, tectonic regimes and high-temperature geothermal systems in fault zones. *Comptes Rendus Geoscience*, 356(S2), 1–33. <https://doi.org/10.5802/crgeos.213>
- Hall, S., Farber, D., Audin, L., & Finkel, R. (2012). Recently active contractile deformation in the forearc of Southern Peru. *Earth and Planetary Science Letters*, 337, 85–92. <https://doi.org/10.1016/j.epsl.2012.04.007>
- Hall, S., Farber, D., Audin, L., Finkel, R., & Mériaux, A.-S. (2008). Geochronology of pediment surfaces in southern Peru: Implications for Quaternary deformation of the Andean forearc. *Tectonophysics*, 459(1–4), 186–205. <https://doi.org/10.1016/j.tecto.2007.11.073>
- Hamza, V. M., Dias, F. J. S., Gomes, A. J., & Terceros, Z. G. D. (2005). Numerical and functional representations of regional heat flow in South America. *Physics of the Earth and Planetary Interiors*, 152(4), 223–256. <https://doi.org/10.1016/j.pepi.2005.04.009>
- Herrera, C., Gamboa, C., Custodio, E., Jordan, T., Godfrey, L., Jódar, J., et al. (2018). Groundwater origin and recharge in the hyperarid Cordillera de la Costa, Atacama Desert, northern Chile. *Science of the Total Environment*, 624, 114–132. <https://doi.org/10.1016/j.scitotenv.2017.12.134>
- Hiett, C. D., Newell, D. L., Jessup, M. J., Grambling, T. A., Scott, B. E., & Upin, H. E. (2022). Deep CO₂ and N₂ emissions from Peruvian hot springs: Stable isotopic constraints on volatile cycling in a flat-slab subduction zone. *Chemical Geology*, 595, 120787. <https://doi.org/10.1016/j.chemgeo.2022.120787>
- Hochstein, M. P. (1988). Assessment and modelling of geothermal reservoirs (small utilization schemes). *Geothermics*, 17(1), 15–49. [https://doi.org/10.1016/0375-6505\(88\)90004-1](https://doi.org/10.1016/0375-6505(88)90004-1)
- Horning, T. S. (1988). The geology, igneous petrology, and mineral deposits of the Atacama mining district, Department of Tacna, Peru. (Unpublished doctoral dissertation). Oregon State University.
- Houston, J., & Hartley, A. J. (2003). The central Andean west-slope rainshadow and its potential contribution to the origin of hyper-aridity in the Atacama Desert. *International Journal of Climatology: A Journal of the Royal Meteorological Society*, 23(12), 1453–1464. <https://doi.org/10.1002/joc.938>
- ICAO. (1993). In *Manual of the ICAO standard atmosphere: Extended to 80 kilometres (262 500 feet)* (Vol. 7488). International Civil Aviation Organization.
- Im, K., Elsworth, D., & Fang, Y. (2018). The influence of preslip sealing on the permeability evolution of fractures and faults. *Geophysical Research Letters*, 45(1), 166–175. <https://doi.org/10.1002/2017GL076216>
- Insel, N., Poulsen, C. J., Ehlers, T. A., & Sturm, C. (2012). Response of meteoric δ¹⁸O to surface uplift—Implications for Cenozoic Andean Plateau growth. *Earth and Planetary Science Letters*, 317, 262–272. <https://doi.org/10.1016/j.epsl.2011.11.039>
- Intani, R. G., Golla, G. U., Syaffitri, Y., Paramitasari, H. M., Nordquist, G. A., Nelson, C., et al. (2020). Improving the conceptual understanding of the Darajat geothermal field. *Geothermics*, 83, 101716. <https://doi.org/10.1016/j.geothermics.2019.101716>
- Jacay, J., Sempere, T., Husson, L., & Pino, A. (2002). Structural characteristics of the Incahuico Fault System, southern Peru. In *International symposium on Andean geodynamics* (Vol. 5, pp. 319–321).

- Jayne, R. S., Pollyea, R. M., Dodd, J. P., Olson, E. J., & Swanson, S. K. (2016). Spatial and temporal constraints on regional-scale groundwater flow in the Pampa del Tamarugal Basin, Atacama Desert, Chile. *Hydrogeology Journal*, 24(8), 1921–1937. <https://doi.org/10.1007/s10040-016-1454-3>
- Jenks, W. F. (1948). Geología de la hoja de Arequipa al 200,000. Geology of the Arequipa Quadrangle of the Carta Nacional del Peru [boletín 9].
- Jolie, E., Scott, S., Faulds, J., Chambeffort, I., Axelsson, G., Gutiérrez-Negrín, L. C., et al. (2021). Geological controls on geothermal resources for power generation. *Nature Reviews Earth & Environment*, 2(5), 324–339. <https://doi.org/10.1038/s43017-021-00154-y>
- Jupp, T. E., & Schultz, A. (2004). Physical balances in seafloor hydrothermal convection cells. *Journal of Geophysical Research*, 109(B5). <https://doi.org/10.1029/2003jb002697>
- Klein, A. G., Seltzer, G. O., & Isacks, B. L. (1999). Modern and last local glacial maximum snowlines in the Central Andes of Peru, Bolivia, and Northern Chile. *Quaternary Science Reviews*, 18(1), 63–84. [https://doi.org/10.1016/S0277-3791\(98\)00095-X](https://doi.org/10.1016/S0277-3791(98)00095-X)
- Kull, C., & Grosjean, M. (2000). Late Pleistocene climate conditions in the north Chilean Andes drawn from a climate-glacier model. *Journal of Glaciology*, 46(155), 622–632. <https://doi.org/10.3189/172756500781832611>
- Labidi, J., Young, E., Fischer, T., Barry, P., Ballentine, C., & de Moor, J. (2021). Recycling of nitrogen and light noble gases in the Central American subduction zone: Constraints from 15N. *Earth and Planetary Science Letters*, 571, 117112. <https://doi.org/10.1016/j.epsl.2021.117112>
- Lahsen, A., Rojas, J., Morata, D., & Aravena, D. (2015). Exploration for high-temperature geothermal resources in the Andean countries of South America. In *Proceedings world geothermal congress* (pp. 19–25).
- Lapwood, E. (1948). Convection of a fluid in a porous medium. In *Mathematical proceedings of the Cambridge philosophical society* (Vol. 44, pp. 508–521). <https://doi.org/10.1017/S030500410002452X>
- Launay, G., Branquet, Y., Sizaret, S., Guillou-Frottier, L., & Gloaguen, E. (2023). How greisenization could trigger the formation of large vein-and-greisen Sn-W deposits: A numerical investigation applied to the Panasqueira deposit. *Ore Geology Reviews*, 153, 105299. <https://doi.org/10.1016/j.oregeorev.2023.105299>
- López, D. L., & Smith, L. (1995). Fluid flow in fault zones: Analysis of the interplay of convective circulation and topographically driven groundwater flow. *Water Resources Research*, 31(6), 1489–1503. <https://doi.org/10.1029/95WR00422>
- Lupi, M., Geiger, S., & Graham, C. (2011). Numerical simulations of seismicity-induced fluid flow in the Tjörnes Fracture Zone, Iceland. *Journal of Geophysical Research*, 116(B7), B07101. <https://doi.org/10.1029/2010JB007732>
- Magaritz, M., Aravena, R., Peña, H., Suzuki, O., & Grilli, A. (1990). Source of ground water in the deserts of northern Chile: Evidence of deep circulation of ground water from the Andes. *Ground Water*, 28(4), 513–517. <https://doi.org/10.1111/j.1745-6584.1990.tb01706.x>
- Magri, F., Möller, S., Inbar, N., Möller, P., Raggad, M., Rödiger, T., et al. (2016). 2D and 3D coexisting modes of thermal convection in fractured hydrothermal systems-implications for transboundary flow in the Lower Yarmouk Gorge. *Marine and Petroleum Geology*, 78, 750–758. <https://doi.org/10.1016/j.marpetgeo.2016.10.002>
- Malkovsky, V., & Magri, F. (2016). Thermal convection of temperature-dependent viscous fluids within three-dimensional faulted geothermal systems: Estimation from linear and numerical analyses. *Water Resources Research*, 52(4), 2855–2867. <https://doi.org/10.1002/2015WR018001>
- Malkovsky, V., & Pek, A. A. (2004). Onset of thermal convection of single-phase fluid in open vertical faults. In *EGS general assembly conference abstracts* (p. 1835).
- Maréchal, J.-C., Perrochet, P., & Tacher, L. (1999). Long-term simulations of thermal and hydraulic characteristics in a mountain massif: The Mont Blanc case study, French and Italian Alps. *Hydrogeology Journal*, 7(4), 341–354. <https://doi.org/10.1007/s100400050207>
- Mariño, J., Samaniego, P., Manrique, N., Valderrama, P., Roche, O., de Vries, B. V. W., et al. (2021). The Tutupaca volcanic complex (Southern Peru): Eruptive chronology and successive destabilization of a dacitic dome complex. *Journal of South American Earth Sciences*, 109, 103227. <https://doi.org/10.1016/j.jsames.2021.103227>
- Moeck, I. S. (2014). Catalog of geothermal play types based on geologic controls. *Renewable and Sustainable Energy Reviews*, 37, 867–882. <https://doi.org/10.1016/j.rser.2014.05.032>
- Moretti, I., Baby, P., Alvarez Zapata, P., & Mendoza, R. V. (2023). Subduction and hydrogen release: The case of Bolivian altiplano. *Geosciences*, 13(4), 109. <https://doi.org/10.3390/geosciences13040109>
- Moretti, I., Labaume, P., Sheppard, S., & Boulegue, J. (2000). Compartmentalisation of fluid flow by thrust faults, sub-Andean Zone, Bolivia. *Journal of Geochemical Exploration*, 69, 493–497. [https://doi.org/10.1016/S0375-6742\(00\)00103-5](https://doi.org/10.1016/S0375-6742(00)00103-5)
- Munoz-Saez, C., Manga, M., Hurwitz, S., Slagter, S., Churchill, D. M., Reich, M., et al. (2020). Radiocarbon dating of silica sinter and postglacial hydrothermal activity in the El Tatio geysir field. *Geophysical Research Letters*, 47(11), e2020GL087908. <https://doi.org/10.1029/2020GL087908>
- NOAA. (2022). National oceanic and atmospheric administration (Vol. 7488). Retrieved from <https://www.noaa.gov/>
- Pardo-Casas, F., & Molnar, P. (1987). Relative motion of the Nazca (Farallon) and South American plates since late Cretaceous time. *Tectonics*, 6(3), 233–248. <https://doi.org/10.1029/TC006i003p00233>
- Parkhurst, D. L., & Appelo, C. (1999). User's guide to PHREEQC (version 2): A computer program for speciation, batch-reaction, one-dimensional transport, and inverse geochemical calculations. *Water-resources investigations report*, 99(4259), 312.
- Pearce, R., Sánchez de la Muela, A., Moorkamp, M., Hammond, J. O., Mitchell, T., Cembrano, J., et al. (2020). Reactivation of fault systems by compartmentalized hydrothermal fluids in the Southern Andes revealed by magnetotelluric and seismic data. *Tectonics*, 39(12), e2019TC005997. <https://doi.org/10.1029/2019TC005997>
- Peña, F., Cotrina Chávez, G. J., & Acosta Pereira, H. (2009). Hidrogeología de la cuenca del río Caplina-Región Tacna. *INGEMMET.Boletín, Serie H: Hidrología*, 1.
- Piper, A. M. (1944). A graphic procedure in the geochemical interpretation of water-analyses. *Eos, Transactions American Geophysical Union*, 25(6), 914–928. <https://doi.org/10.1029/TR025i006p00914>
- Placzek, C., Quade, J., Betancourt, J. L., Patchett, P. J., Rech, J. A., Latorre, C., et al. (2009). Climate in the dry central Andes over geologic, millennial, and interannual timescales. *Annals of the Missouri Botanical Garden*, 96(3), 386–397. <https://doi.org/10.3417/2008019>
- Potter, R., & Brown, D. (1977). The volumetric properties of aqueous sodium chloride solutions from 0°C to 500°C at pressures up to 2000 bars based on a regression of available data in the literature. *US Geological Survey Bulletin*, 1421.
- Prostka, H. J., Moore, J. L., & La Fleur, J. (1982). Geology and geothermal exploration, southernmost Peru. *AAPG Bulletin*, 66(7), 981. <https://doi.org/10.1306/03B5A58E-16D1-11D7-8645000102C1865D>
- Putman, A. L., & Bowen, G. J. (2019). A global database of the stable isotopic ratios of meteoric and terrestrial waters. *Hydrology and Earth System Sciences*, 23(10), 4389–4396. <https://doi.org/10.5194/hess-23-4389-2019>
- Rabinowicz, M., Boulègue, J., & Genthon, P. (1998). Two- and three-dimensional modeling of hydrothermal convection in the sedimented Middle Valley segment, Juan de Fuca Ridge. *Journal of Geophysical Research*, 103(B10), 24045–24065. <https://doi.org/10.1029/98JB01484>

- Rau, P., Bourrel, L., Labat, D., Melo, P., Dewitte, B., Frappart, F., et al. (2017). Regionalization of rainfall over the Peruvian Pacific slope and coast. *International Journal of Climatology*, 37(1), 143–158. <https://doi.org/10.1002/joc.4693>
- Rivera, M., Samaniego, P., Vela, J., Le Pennec, J.-L., Guillou, H., Paquette, J.-L., & Liorzou, C. (2020). The eruptive chronology of the Yucamane-Calientes compound volcano: A potentially active edifice of the central Andes (southern Peru). *Journal of Volcanology and Geothermal Research*, 393, 106787. <https://doi.org/10.1016/j.jvolgeores.2020.106787>
- Rowe, C. D., Meneghini, F., & Moore, J. C. (2009). Fluid-rich damage zone of an ancient out-of-sequence thrust, Kodiak Islands, Alaska. *Tectonics*, 28(1). <https://doi.org/10.1029/2007TC002126>
- Sakai, H., & Matsubaya, O. (1977). Stable isotopic studies of Japanese geothermal systems. *Geothermics*, 5(1–4), 97–124. [https://doi.org/10.1016/0375-6505\(77\)90014-1](https://doi.org/10.1016/0375-6505(77)90014-1)
- Sánchez-Murillo, R., Aguirre-Dueñas, E., Gallardo-Amestica, M., Moya-Vega, P., Birkel, C., Esquivel-Hernández, G., & Boll, J. (2018). Isotopic characterization of waters across Chile. *Andean hydrology*, 1, 203–225. <https://doi.org/10.1201/9781315155982-9>
- Santoyo, E., & Díaz-González, L. (2010). A new improved proposal of the Na/K geothermometer to estimate deep equilibrium temperatures and their uncertainties in geothermal systems. In *Proceedings world geothermal congress, Bali, Indonesia* (pp. 25–29).
- Savage, H. M., & Brodsky, E. E. (2011). Collateral damage: Evolution with displacement of fracture distribution and secondary fault strands in fault damage zones. *Journal of Geophysical Research*, 116(B3), B03405. <https://doi.org/10.1029/2010jb007665>
- Scheihing, K. W., Moya, C. E., & Tröger, U. (2017). Insights into Andean slope hydrology: Reservoir characteristics of the thermal Pica spring system, Pampa del Tamarugal, northern Chile. *Hydrogeology Journal*, 25(6), 1833–1852. <https://doi.org/10.1007/s10040-017-1533-0>
- Schepers, G., Van Hinsbergen, D. J., Spakman, W., Kosters, M. E., Boschman, L. M., & McQuarrie, N. (2017). South-American plate advance and forced Andean trench retreat as drivers for transient flat subduction episodes. *Nature Communications*, 8(1), 15249. <https://doi.org/10.1038/ncomms15249>
- Scott, B. E., Newell, D. L., Jessup, M., Grambling, T., & Shaw, C. (2020). Structural controls on crustal fluid circulation and hot spring geochemistry above a flat-slab subduction zone, Peru. *Geochemistry, Geophysics, Geosystems*, 21(7), e2020GC008919. <https://doi.org/10.1029/2020GC008919>
- Sibson, R. H. (1981). Fluid flow accompanying faulting: Field evidence and models. *Earthquake prediction: An. International Review*, 4, 593–603. <https://doi.org/10.1029/ME004p0593>
- Simler, R. (2014). Diagrammes v6.77. Retrieved from <http://www.lha.univ-avignon.fr/LHA-Logiciels.htm>
- Smeraglia, L., Fabbri, O., Choulet, F., Jaggi, M., & Bernasconi, S. M. (2022). The role of thrust and strike-slip faults in controlling regional-scale paleofluid circulation in fold-and-thrust belts: Insights from the Jura Mountains (eastern France). *Tectonophysics*, 829, 229299. <https://doi.org/10.1016/j.tecto.2022.229299>
- Sonney, R., & Vuataz, F.-D. (2009). Numerical modelling of alpine deep flow systems: A management and prediction tool for an exploited geothermal reservoir (Lavey-les-Bains, Switzerland). *Hydrogeology Journal*, 17(3), 601–616. <https://doi.org/10.1007/s10040-008-0394-y>
- Stelling, P., Shevenell, L., Hinz, N., Coolbaugh, M., Melosh, G., & Cumming, W. (2016). Geothermal systems in volcanic arcs: Volcanic characteristics and surface manifestations as indicators of geothermal potential and favorability worldwide. *Journal of Volcanology and Geothermal Research*, 324, 57–72. <https://doi.org/10.1016/j.jvolgeores.2016.05.018>
- Sutherland, R., Townend, J., Toy, V., Upton, P., Coussens, J., Allen, M., et al. (2017). Extreme hydrothermal conditions at an active plate-bounding fault. *Nature*, 546(7656), 137–140. <https://doi.org/10.1038/nature22355>
- Taillefer, A., Guillou-Frotier, L., Soliva, R., Magri, F., Lopez, S., Courrioux, G., et al. (2018). Topographic and faults control of hydrothermal circulation along dormant faults in an orogen. *Geochemistry, Geophysics, Geosystems*, 19(12), 4972–4995. <https://doi.org/10.1029/2018GC007965>
- Taillefer, A., Milesi, G., Soliva, R., Monnier, L., Delorme, P., Guillou-Frotier, L., & Le Goff, E. (2021). Polyphased brittle deformation around a crustal fault: A multi-scale approach based on remote sensing and field data on the mountains surrounding the Têt hydrothermal system (eastern Pyrénées, France). *Tectonophysics*, 804, 228710. <https://doi.org/10.1016/j.tecto.2020.228710>
- Taillefer, A., Truche, L., Audin, L., Donzé, F., Tisserand, D., Denti, S., et al. (2024). Geochemical characterization of hot springs in the Tacna region (18°S, Peru), Version 1.0. [Dataset]. *IEDA*. <https://doi.org/10.60520/IEDA/113186>
- Tassi, F., Aguilera, F., Darrah, T., Vaselli, O., Capaccioni, B., Poreda, R., & Huertas, A. D. (2010). Fluid geochemistry of hydrothermal systems in the Arica-Parinacota, Tarapacá and Antofagasta regions (northern Chile). *Journal of Volcanology and Geothermal Research*, 192(1–2), 1–15. <https://doi.org/10.1016/j.jvolgeores.2010.02.006>
- Tavera, H., Audin, L., & Bernal Esquia, Y. I. (2007). Parámetros de la fuente del sismo de Sama (Tacna), 20 de noviembre de 2006 (5.4 Mw). *Boletín de la Sociedad Geologica del Peru*.
- Thouret, J.-C., Wörner, G., Gunnell, Y., Singer, B., Zhang, X., & Souriot, T. (2007). Geochronologic and stratigraphic constraints on canyon incision and Miocene uplift of the Central Andes in Peru. *Earth and Planetary Science Letters*, 263(3–4), 151–166. <https://doi.org/10.1016/j.epsl.2007.07.023>
- Torabi, A., & Berg, S. S. (2011). Scaling of fault attributes: A review. *Marine and Petroleum Geology*, 28(8), 1444–1460. <https://doi.org/10.1016/j.marpetgeo.2011.04.003>
- Tyc, A., Gaidzik, K., Ciesielczuk, J., Masías, P., Paulo, A., Postawa, A., & Žaba, J. (2022). Thermal springs and active fault network of the central Colca River basin, Western Cordillera, Peru. *Journal of Volcanology and Geothermal Research*, 424, 107513. <https://doi.org/10.1016/j.jvolgeores.2022.107513>
- Urrutia, J., Herrera, C., Custodio, E., Jódar, J., & Medina, A. (2019). Groundwater recharge and hydrodynamics of complex volcanic aquifers with a shallow saline lake: Laguna Tuyajto, Andean Cordillera of northern Chile. *Science of the Total Environment*, 697, 134116. <https://doi.org/10.1016/10.1016/j.scitotenv.2019.134116>
- Van Zalinge, M., Sparks, R., Evenstar, L., Cooper, F., Aslin, J., & Condon, D. (2017). Using ignimbrites to quantify structural relief growth and understand deformation processes: Implications for the development of the Western Andean Slope, northernmost Chile. *Lithosphere*, 9(1), 29–45. <https://doi.org/10.1130/L593.1>
- Vargas, V., & Cruz, V. (2010). Geothermal map of Perú. *World Geothermal Congress*, 2010.
- Veloso, E. E., Tardani, D., Elizalde, D., Godoy, B. E., Sánchez-Alfaro, P. A., Aron, F., et al. (2020). A review of the geodynamic constraints on the development and evolution of geothermal systems in the Central Andean Volcanic Zone (18–28 lat.S). *International Geology Review*, 62(10), 1294–1318. <https://doi.org/10.1080/00206814.2019.1644678>
- Vera, A., Pino-Vargas, E., Verma, M. P., Chucuya, S., Chávarri, E., Canales, M., et al. (2021). Hydrodynamics, hydrochemistry, and stable isotope geochemistry to assess temporal behavior of seawater intrusion in the la Yarada aquifer in the vicinity of Atacama desert, Tacna, Peru. *Water*, 13(22), 3161. <https://doi.org/10.3390/w13223161>
- Vieira, F., & Hamza, V. (2019). Assessment of geothermal resources of South America—a new look. *International Journal of Terrestrial Heat Flow and Applied Geothermics*, 2(1), 46–57. <https://doi.org/10.31214/ijthfa.v2i1.32>

- Vigui er, B., Daniele, L., Jourde, H., Leonardi, V., & Y a nez, G. (2019). Changes in the conceptual model of the Pampa del Tamarugal Aquifer: Implications for Central Depression water resources. *Journal of South American Earth Sciences*, *94*, 102217. <https://doi.org/10.1016/j.jsames.2019.102217>
- Villegas-Lanza, J. C., Chlieh, M., Cavali e, O., Tavera, H., Baby, P., Chire-Chira, J., & Nocquet, J.-M. (2016). Active tectonics of Peru: Heterogeneous interseismic coupling along the Nazca megathrust, rigid motion of the Peruvian Sliver, and Subandean shortening accommodation. *Journal of Geophysical Research: Solid Earth*, *121*(10), 7371–7394. <https://doi.org/10.1002/2016JB013080>
- Volpi, G., Magri, F., Frattini, P., Crosta, G. B., & Riva, F. (2017). Groundwater-driven temperature changes at thermal springs in response to recent glaciation: Bormio hydrothermal system, Central Italian Alps. *Hydrogeology Journal*, *25*(7), 1967–1984. <https://doi.org/10.1007/s10040-017-1600-6>
- Wanner, C., Diamond, L. W., & Alt-Epping, P. (2019). Quantification of 3-D thermal anomalies from surface observations of an orogenic geothermal system (Grimsel Pass, Swiss Alps). *Journal of Geophysical Research: Solid Earth*, *124*(11), 10839–10854. <https://doi.org/10.1029/2019JB018335>
- Wanner, C., Waber, H. N., & Bucher, K. (2020). Geochemical evidence for regional and long-term topography-driven groundwater flow in an orogenic crystalline basement (Aar Massif, Switzerland). *Journal of Hydrology*, *581*, 124374. <https://doi.org/10.1016/j.jhydrol.2019.124374>
- Ward, D., Thornton, R., & Cesta, J. (2017). Across the Arid Diagonal: Deglaciation of the western Andean Cordillera in southwest Bolivia and northern Chile. Cuadernos de investigaci on geogr fica. *Geographical Research Letters*, *43*(43), 667–696. <https://doi.org/10.18172/cig.3209>
- White, D. E. (1965). Saline waters of sedimentary rocks. *Fluids in Subsurface Environments*. <https://doi.org/10.1306/M4360C14>
- Wilson, C. J., & Rowland, J. V. (2016). The volcanic, magmatic and tectonic setting of the Taupo Volcanic Zone, New Zealand, reviewed from a geothermal perspective. *Geothermics*, *59*, 168–187. (Taupo Volcanic Zone Geothermal Systems, New Zealand: Exploration, Science and Development). <https://doi.org/10.1016/j.geothermics.2015.06.013>
- Wilson, J. J., & Garc a, W. (1962). Geolog a de los cuadr ngulos de Pach a y Palca. Hojas 36-vy 36-x)-[Bolet n a 4].
- W rner, G., Hammerschmidt, K., Henjes-Kunst, F., Lezaun, J., & Wilke, H. (2000). Geochronology (40Ar/39Ar, K-Ar and He-exposure ages) of Cenozoic magmatic rocks from northern Chile (18–22 s): Implications for magmatism and tectonic evolution of the central Andes. *Revista Geologica de Chile*, *27*(2), 205–240.
- Wrage, J., Tardani, D., Reich, M., Daniele, L., Arancibia, G., Cembrano, J., et al. (2017). Geochemistry of thermal waters in the Southern Volcanic Zone, Chile—Implications for structural controls on geothermal fluid composition. *Chemical Geology*, *466*, 545–561. <https://doi.org/10.1016/j.chemgeo.2017.07.004>
- Zerathe, S., Audin, L., Robert, X., Schwartz, S., & Carcaillet, J. (2023). Large landslide of the hyperarid Central Western Andes triggered during a humid period of the Late Pleistocene (ca. 19° S; northern Chile). *Terra Nova*, *35*(3), 174–184. <https://doi.org/10.1111/ter.12641>
- Zerathe, S., Blard, P.-H., Braucher, R., Bourl es, D., Audin, L., Carcaillet, J., et al. (2017). Toward the feldspar alternative for cosmogenic 10Be applications. *Quaternary Geochronology*, *41*, 83–96. <https://doi.org/10.1016/j.quageo.2017.06.004>